The Astrophysical Journal, 809:57 (16pp), 2015 August 10 doi:10.1088/0004-637X/809/1/57
© 2015. The American Astronomical Society. All rights reserved.

EFFECT OF UV RADIATION ON THE SPECTRAL FINGERPRINTS OF EARTH-LIKE PLANETS ORBITING M STARS

S. Rugheimer[1,2], L. Kaltenegger[2,3], A. Segura[4], J. Linsky[5], and S. Mohanty[6]
[1] Harvard Smithsonian Center for Astrophysics, 60 Garden Street, Cambridge, MA 02138, USA
[2] Carl Sagan Institute, Cornell University, Ithaca, NY 14853, USA
[3] MPIA, Koenigstuhl 17, D-69117 Heidelberg, Germany
[4] Instituto de Ciencias Nucleares, Universidad Nacional Autónoma de México, México
[5] JILA, University of Colorado and NIST, 440 UCB, Boulder, CO 80309-0440, USA
[6] Imperial College London, 1010 Blackett Lab, Prince Consort Road, London SW7 2AZ, UK
Received 2014 August 18; accepted 2015 June 10; published 2015 August 10

ABSTRACT

We model the atmospheres and spectra of Earth-like planets orbiting the entire grid of M dwarfs for active and inactive stellar models with $T_{\rm eff} = 2300$ K to $T_{\rm eff} = 3800$ K and for six observed MUSCLES M dwarfs with UV radiation data. We set the Earth-like planets at the 1 AU equivalent distance and show spectra from the visible to IR (0.4–20 μm) to compare detectability of features in different wavelength ranges with the *James Webb Space Telescope* and other future ground- and spaced-based missions to characterize exo-Earths. We focus on the effect of UV activity levels on detectable atmospheric features that indicate habitability on Earth, namely, H_2O, O_3, CH_4, N_2O, and CH_3Cl. To observe signatures of life—O_2/O_3 in combination with reducing species like CH_4—we find that early and active M dwarfs are the best targets of the M star grid for future telescopes. The O_2 spectral feature at 0.76 μm is increasingly difficult to detect in reflected light of later M dwarfs owing to low stellar flux in that wavelength region. N_2O, another biosignature detectable in the IR, builds up to observable concentrations in our planetary models around M dwarfs with low UV flux. CH_3Cl could become detectable, depending on the depth of the overlapping N_2O feature. We present a spectral database of Earth-like planets around cool stars for directly imaged planets as a framework for interpreting future light curves, direct imaging, and secondary eclipse measurements of the atmospheres of terrestrial planets in the habitable zone to design and assess future telescope capabilities.

Key words: astrobiology – planets and satellites: atmospheres – planets and satellites: terrestrial planets – stars: low-mass

1. INTRODUCTION

About 2000 extrasolar planets have been found to date, with thousands more awaiting confirmation from space- and ground-based searches. Several of these planets have been found in or near the circumstellar habitable zone (see, e.g., Udry et al. 2007; Borucki et al. 2011, 2013; Kaltenegger & Sasselov 2011; Batalha et al. 2013; Kaltenegger et al. 2013; Quintana et al. 2014), with masses and radii consistent with rocky planet models. Future mission concepts to characterize Earth-like planets are designed to take spectra of extrasolar planets with the ultimate goal of remotely detecting atmospheric signatures (e.g., Beichman et al. 1999, 2006; Cash 2006; Kaltenegger et al. 2006; Traub et al. 2006). Several proposed missions are designed to characterize nearby super-Earth and Earth-like planets using emergent visible and infrared spectra. For transiting terrestrial planets, the *James Web Space Telescope* (*JWST*; see Gardner et al. 2006; Deming et al. 2009; Kaltenegger & Traub 2009), as well as future ground- and space-based telescopes (Snellen et al. 2013; Rodler and López-Morales 2014), will search for biosignatures in a rocky planet's atmosphere. NASA's explorer mission *Transiting Exoplanet Survey Satellite* (*TESS*) is designed to search the whole sky for potentially habitable planets around the closest and brightest stars to Earth (et al. 2014), for eventual follow-up with *JWST* and large ground-based observatories such as the E-ELT or GMT.

In our solar neighborhood, 75% of stars are M dwarfs. The abundance of M dwarfs, as well as the contrast ratio and transit probability, favors the detection of planets in the habitable zone of M dwarfs. Therefore, it is likely that the first habitable planet suitable for follow-up observations will be found orbiting a nearby M dwarf (Dressing & Charbonneau 2013). The M spectral class is very diverse, spanning nearly three orders of magnitude in luminosity and an order of magnitude in mass.

The UV environment of a host star dominates the photochemistry and therefore the resulting atmospheric constituents, including biosignatures for terrestrial planets (see, e.g., Segura et al. 2005; Hu et al. 2012; Rugheimer et al. 2013; Domagal-Goldman et al. 2014; Grenfell et al. 2014; Tian et al. 2014). To date, few observations exist in the UV region for M dwarfs. Previously, only UV spectra of very active flare stars, such as AD Leo, were available from the *IUE* satellite, primarily during flares and for a few quiescent phases. The MUSCLES program observed chromospheric emission from six weakly active M dwarfs with *Hubble Space Telescope* (*HST*; France et al. 2013). Note that Lyα is by far the strongest line in the UV for M dwarfs. Since the core of the intrinsic stellar Lyα emission is absorbed by neutral hydrogen in the interstellar medium, one must reconstruct the line to compensate for this absorption to get accurate flux levels (see, e.g., Wood et al. 2005; Linsky et al. 2013).

Several groups have explored the effect of a different stellar spectral type on the atmospheric composition of Earth-like planets by primarily considering one star, AD Leo, as a template for the diverse range of M dwarfs, and by using the extreme limit of inactivity, photosphere-only, PHOENIX models (Segura et al. 2005; Kitzmann et al. 2011a, 2011b;

Wordsworth et al. 2011; Grenfell et al. 2014). In this paper we expand on this work by establishing planetary atmosphere models for the full M dwarf main sequence, using a stellar temperature grid from 3800 to 2400 K, including recent *HST* observations of six M dwarfs to explore the effect of different spectral energy distributions (SEDs) on terrestrial atmosphere models and on detectable atmospheric signatures, including biosignatures. Atmospheric biosignatures are remotely detectable chemical species in the atmosphere that are by-products of life processes. Recent research shows that possible false positives may occur under certain geological settings (Domagal-Goldman et al. 2014; Tian et al. 2014; Wordsworth & Pierrehumbert 2014).

We create a grid of M dwarf input spectra, which can be used to probe the entire range of UV flux levels. To showcase the whole range, we simulate model planets around host stars at the two extreme limits of activity: active and inactive stellar models. We compare these models to the six observed M dwarfs with recent UV observations (France et al. 2013).

We explore the influence of stellar UV flux on the atmospheric structure, chemical abundance, and spectral features for Earth-like planets, including the observability of biosignatures in the visible to IR. We focus our analysis on spectral biosignatures for a temperate rocky planet like Earth, O_3, O_2, CH_4, N_2O, and CH_3Cl, and those that indicate habitability, H_2O and CO_2 (Lovelock 1975; Sagan et al. 1993; Des Marais et al. 2002).

In Section 2, we describe our model, and Section 3 presents the influence of stellar types on the abundance of atmospheric chemical species. In Section 4, we examine the remote observability of such spectral features, and in Sections 5 and 6, we summarize the results and discuss their implications.

2. MODEL DESCRIPTION

2.1. Stellar M Dwarf Spectral Grid Model

M dwarfs span nearly three orders of magnitude in luminosity and remain active for much longer timescales than earlier stellar types. As main-sequence stars age, their UV flux levels decrease even as their bolometric luminosity increases. Understanding the UV flux incident on a planetary atmosphere is critical to understanding and interpreting future observations of atmospheric constituents, including biosignatures.

Current stellar models are unable to model the UV region from M dwarfs self-consistently for three main reasons. First, complex magnetic fields responsible for heating the chromosphere are thought to drive much of the UV activity and have thus far been ignored in stellar models. Second, the models are missing opacities in the UV. Third, the models are semi-empirical, with no energy conservation to balance magnetic heating with radiative losses. These problems are being addressed by current work, and models will be available in the future to test against M dwarf UV observations.

We generate stellar input models for the entire M dwarf spectral class (M0 to M9) to explore the boundaries of the UV environment of an exoplanet orbiting a main-sequence star. We create two sets of models based on the extreme limits of stellar activity. For the purposes of this paper, "active" stellar models are constructed to represent the most active M dwarf measurements, and "inactive" semi-empirical models without chromospheres are constructed to represent the lowest theoretical UV flux field. We compare these limiting-case models with six well-observed M dwarfs that show significant chromospheric flux (see Figure 1) despite being traditionally classified as quiescent stars owing to the presence of Hα in absorption (France et al. 2013). A few M dwarfs observed with *GALEX* in the near-ultraviolet (near-UV; 1750–2750 Å) show near-photospheric continuum level fluxes (as computed with PHOENIX models) and can be classified as inactive even though the exact UV flux level has not been measured yet. For example, Gl 445 and Gl 682 have roughly 90% of the observed NUV flux density predicted by PHOENIX model photospheres (Shkolnik & Barman 2014). More observations are needed to determine the ultimate lower limit of UV flux emitted by old and/or late M dwarfs. To compare our calculations for inactive star models with published work, we use theoretical photosphere PHOENIX models as a lower bound (Allard 2014).

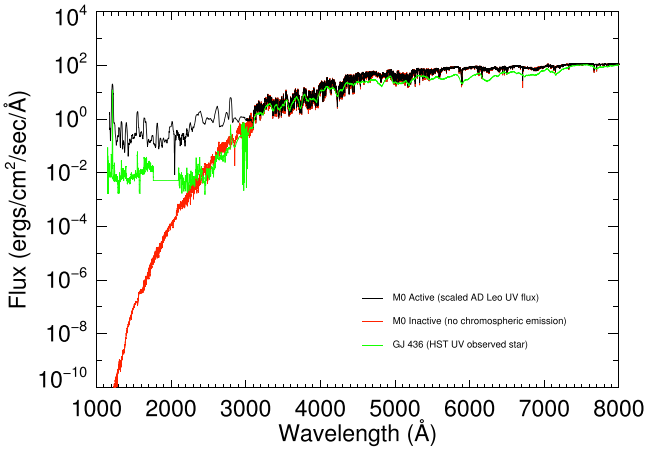


Figure 1. Stellar input spectra at the top of the atmosphere (TOA) of Earth-like planets at the 1 AU equivalent of an M0 "active" star with UV flux scaled from AD Leo (black), "inactive" PHOENIX model of M0, and *HST* UV observations plus photosphere model for GJ 436 (green).

The chromospheric far-ultraviolet (far-UV) flux from M, L, and T dwarfs (i.e., very low mass stars and brown dwarfs), while crucial for determining the potential habitability of any planets around them, is very poorly characterized through direct observations. Given their common chromospheric origin, Hα, Lyα, Ca II H and K, and Mg II H and K emission lines have all been used as proxies for FUV activity. However, many of these lines are inaccessible to M dwarfs because they are at shorter wavelengths, where these stars are intrinsically less luminous. For M dwarfs, Hα emission, in particular, has been studied extensively and to date has the most robust data set for each M dwarf spectral type compared with the other lines considered above (West et al. 2004, 2011). In addition, Jones & West (2015) shows that Hα fluxes correlate with NUV fluxes from *GALEX*. Therefore, we use Hα to estimate the FUV emission for our active stellar grid by scaling the known FUV and Hα emission from the active M3.5 star AD Leo (see Equation (1) and Figure 2). Very active, early M dwarfs (M0–M5) are known to saturate in the Hα emission around $\log(L_{H_\alpha}/L_{bol}) = -3.75$ (Hawley et al. 1996; West et al. 2004; Reiners & Basri 2008).

West et al. (2004) tabulate the $\log(\text{mean } L_{H_\alpha}/L_{bol})$ versus spectral type from M0 to L0 from observations of 1910 active M dwarfs. We parameterize the data from West et al. (2004) to derive a relationship of UV to mean Hα emission for each spectral subtype in the M dwarf class (see Figure 2 and

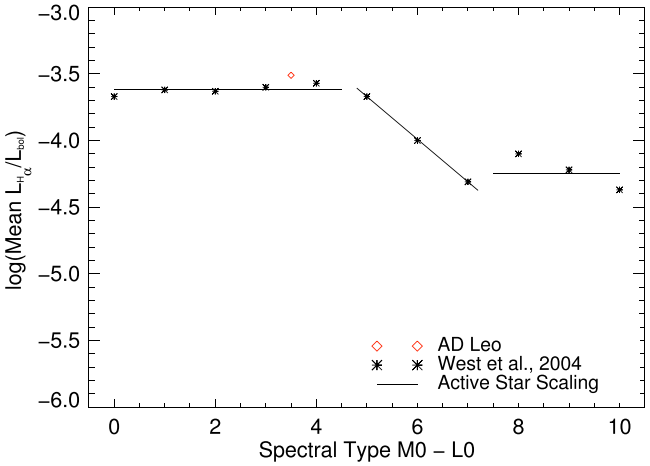


Figure 2. Scaling used for active stellar models (black line) overplotted on West et al. (2004) measurements of log (mean L_{H_α}/L_{bol}) (black asterisks).

Equation (1)):

$$\log\left(L_{H_\alpha *}/L_{bol*}\right) = -3.62 \text{ for M0–M4}$$
$$\log\left(L_{H_\alpha *}/L_{bol*}\right) = -0.32 \times (M) - 2.07$$
$$\text{where } M = 5, 6, 7 \text{ for M5, M6, M7}$$
$$\log\left(L_{H_\alpha *}/L_{bol*}\right) = -4.25 \text{ for M8–M9}. \quad (1)$$

We use the Hα/UV scaling of AD Leo, which has both a well-characterized UV spectrum and Hα emission measurement as a calibration data point to set the scale. AD Leo, an M3.5 eV star, has $\log(L_{H_\alpha}/L_{bol}) = -3.51$ (Walkowicz & Hawley 2009) and has been well observed in the UV (see Segura et al. 2005 for AD Leo *IUE* spectrum and Linsky et al. 2013 for reconstructed Lyα flux). The M dwarf active spectrum is then given by

$$F_{FUV*} = F_{FUV\ AD\ Leo} \times \left(\frac{T_{eff\ *}}{T_{eff\ AD\ Leo}}\right)^4 \times \frac{\log\left(L_{H_\alpha *}/L_{bol*}\right)}{\log\left(L_{H_\alpha ADLeo}/L_{bolADLeo}\right)}. \quad (2)$$

Our stellar temperature grid (Figure 3) covers the full M dwarf spectral range, with the stellar parameters for active and inactive models given in Table 1. For the active star models, we scale the UV flux in the wavelength range 1000–3000 Å from AD Leo's observed UV spectrum to the other spectral types according to Equation (2). For each active model star on our grid we concatenated a solar-metallicity, unreddened synthetic PHOENIX spectrum, which only considers photospheric emission (Allard 2014), from 3000 to 45450 Å to the scaled observations from the *IUE* archive for AD Leo from 1000 to 3000 Å combined with the reconstructed Lyα from Linsky et al. (2013) for the region 1210–1222 Å.[7] Note that young active stars are highly variable, especially in the UV. AD Leo is the most active and well-characterized M dwarf. Our active models therefore represent the extreme high end of activity for each stellar type from an active flare star. For comparison, the inactive semi-empirical models include no chromospheric emission. The continuum originating from the photosphere is taken from a PHOENIX model with the same stellar parameters as the corresponding active star from 1000–45450 Å. Thus, these models provide only a lower limit to the stellar UV flux. More observations are needed to determine the true lower limit of inactive M dwarfs in the UV.

The models represent the extreme limits of the UV radiation environment for an exoplanet using a flare star for the upper bound and a photosphere-only model for the lower bound in the UV. Figure 1 shows that the UV flux region between those two limits spans over 10 orders of magnitude in the FUV. We use the observations of six M dwarfs from the MUSCLES program to probe the region in between our active and inactive models. The MUSCLES stars have been traditionally classified as "quiescent" because they do not present Hα in emission.

The six M dwarfs were observed by two UV spectrographs (COS and STIS) on *HST* (France et al. 2013). We joined these *HST* measurements[8] with the star's corresponding PHOENIX models at 2800 Å after adjusting the *HST* flux levels to the level a planet would receive at the 1 AU equivalent in the habitable zone. The input parameters for the PHOENIX models are the observed star's T_{eff}, [Fe/H], log g, and the rotation velocity, v sin i, as summarized in Table 2 and described for each star based on the most recent observations in the Appendix. When observations of v sin i were not available, we used instead the peak of the observed distribution for 56 M dwarfs (Jenkins et al. 2009).

The MUSCLES database interpolates the region between 1760 and 2100 Å because the noise in the observations was large in that region since those wavelengths were covered by the lowest-sensitivity part of the STIS G230L bandpass. In order to not bias the results too high or too low, the MUSCLES team used the average flux in the 2100–2200 Å region to interpolate the 1760–2100 Å region. Follow-up observations to the MUSCLES program with a new *HST* Treasury program aim to probe the 1760–2100 Å region of the spectrum with higher sensitivity. We used the MUSCLES database and interpolation as given. Because this region of the UV is important for O_3 production, uncertainty of this interpolation could influence our atmospheric results.

Input active stellar spectra and MUSCLES spectra are shown in Figure 3 (inactive models are not shown).

2.2. Planetary Atmosphere Model

We use EXO-P (Kaltenegger & Sasselov 2010), a coupled 1D radiative-convective atmosphere code developed for rocky exoplanets. The code incorporates a 1D climate (Kasting & Ackerman 1986; Pavlov et al. 2000; Haqq-Misra et al. 2008), 1D photochemistry (Pavlov & Kasting 2002; Segura et al. 2005, 2007) and 1D radiative transfer model (Traub & Stier 1976; Kaltenegger & Traub 2009) to calculate the model spectrum of an Earth-like exoplanet orbiting host M dwarfs in the habitable zone.

EXO-P is a model that simulates both the effects of stellar radiation on a planetary environment and the planet's outgoing spectrum. We model an altitude range that extends upward to 60 km with 100 height layers. We use a geometrical model in which the average 1D global atmospheric model profile is

[7] http://archive.stsci.edu/iue/

[8] http://cos.colorado.edu/~kevinf/muscles.html

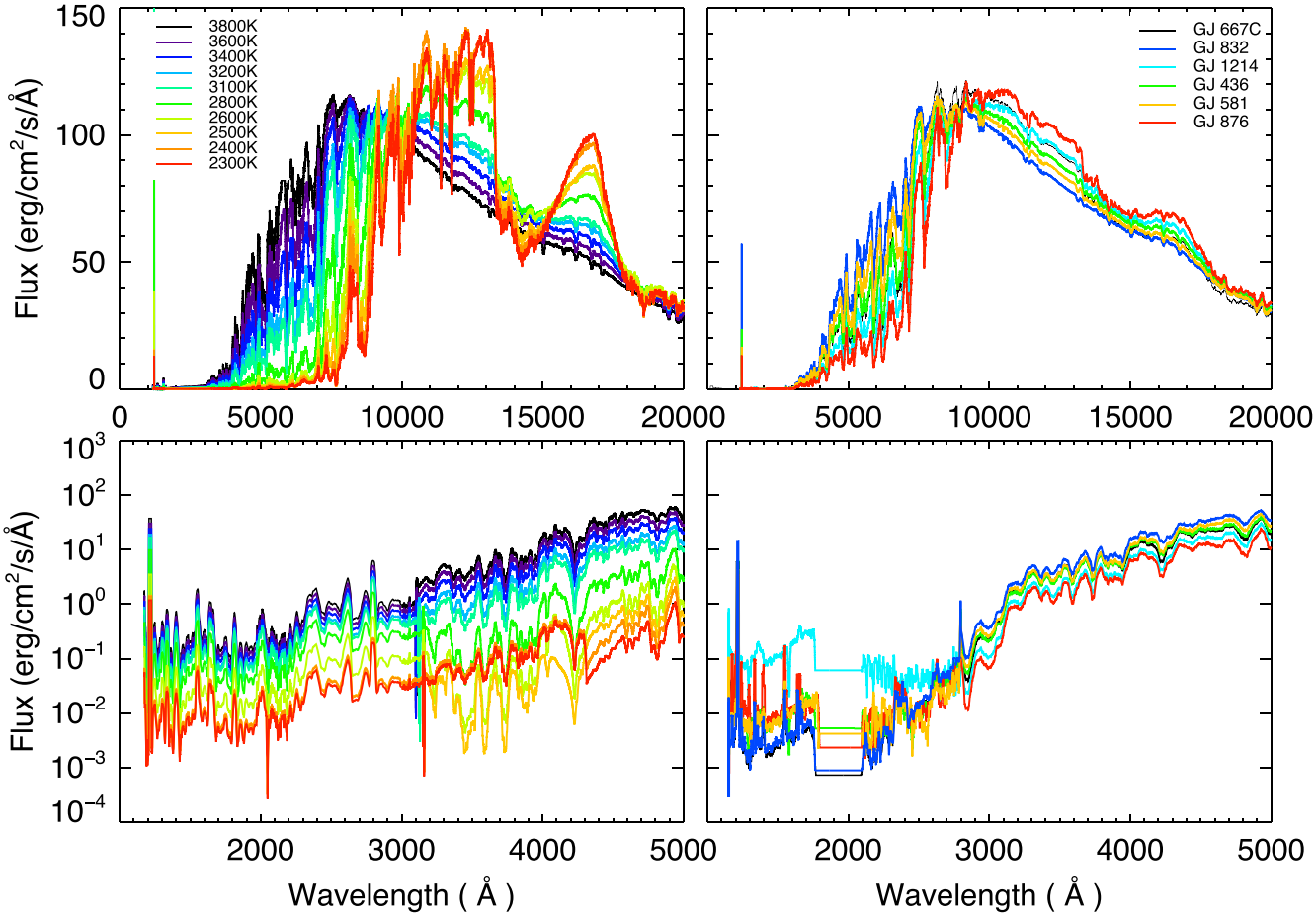


Figure 3. Top: stellar input spectra from 1000 to 20000 Å for the M0–M9 active grid stars with UV scaled by H_α and AD Leo UV flux (left) and MUSCLES stars with *HST* UV observations (right). Bottom: UV input stellar fluxes in log scale.

Table 1
Stellar Properties for Active and Inactive Models

Star	$T_{\rm eff}$ (K)	Mass ($M_\odot$)	Radius ($R_\odot$)
M0	3800	0.60	0.62
M1	3600	0.49	0.49
M2	3400	0.44	0.44
M3	3200	0.36	0.39
M4	3100	0.2	0.36
M5	2800	0.14	0.2
M6	2600	0.10	0.15
M7	2500	0.09	0.12
M8	2400	0.08	0.11
M9	2300	0.075	0.08

generated using a plane-parallel atmosphere, treating the planet as a Lambertian sphere, and setting the stellar zenith angle to 60° to represent the average incoming stellar flux on the dayside of the planet (see also Schindler & Kasting 2000). The temperature in each layer is calculated from the difference between the incoming and outgoing flux and the heat capacity of the atmosphere in each layer. If the lapse rate of a given layer is larger than the adiabatic lapse rate, it is adjusted to the adiabatic rate until the atmosphere reaches equilibrium. We use a two-stream approximation (see Toon et al. 1989), which includes multiple scattering by atmospheric gases, in the visible/near-IR (NIR) to calculate the short-wave fluxes. Four-term, correlated-*k* coefficients parameterize the absorption by O_3, H_2O, O_2, and CH_4 (Pavlov et al. 2000). In the thermal IR region, a rapid radiative transfer model calculates the long-wave fluxes. Clouds are not explicitly calculated. The effects of clouds on the temperature versus pressure profile are included by adjusting the surface albedo of the Earth–Sun system to have a surface temperature of 288 K (see Kasting et al. 1984; Pavlov et al. 2000; Segura et al. 2003, 2005). The photochemistry code, originally developed by Kasting et al. (1985), solves for 55 chemical species linked by 220 reactions using a reverse-Euler method (see Segura et al. 2010, and references therein). The photochemical model is stationary, and convergence is achieved when the following criteria are fulfilled: the production and loss rates of chemical species are balanced, which results in a steady state for the chemical concentrations, and the initial boundary conditions, such as surface mixing ratios or surface fluxes, are met.

The radiative transfer model used to compute planetary spectra is based on a model originally developed for trace gas retrieval in Earth's atmospheric spectra (Traub & Stier 1976) and further developed for exoplanet transmission and emergent spectra (Kaltenegger et al. 2007, 2013; Kaltenegger & Traub 2009; Kaltenegger 2010; Kaltenegger & Sasselov 2010). In this paper, we model Earth's reflected and thermal emission spectra using 21 of the most spectroscopically significant molecules (H_2O, O_3, O_2, CH_4, CO_2, OH, CH_3Cl, NO_2, N_2O, HNO_3, CO, H_2S, SO_2, H_2O_2, NO, ClO, HOCl, HO_2, H_2CO, N_2O_5, and HCl). We use a Lambert sphere as an approximation for the disk-integrated planet in our model. The surface of our

Table 2
Stellar Properties for MUSCLES Model Stellar Spectra

MUSCLES Stars	$T_{\rm eff}$ (K)	Radius ($R_\odot$)	[Fe/H]	log g	Age (Gyr)	v sin i (km s^{-1})
GJ 832	3620	0.48	–0.12	4.70	···	3
GJ 667C	3350	0.348	–0.55	5.00	>2	3
GJ 1214	3250	0.211	+0.05	4.99	6 ± 3	<1
GJ 436	3416	0.455	+0.04	4.83	6.5–9.9	< 1
GJ 581	3498	0.299	–0.10	4.96	7–11	2.1
GJ 876	3129	0.3761	+0.19	4.89	0.1–5	1.38

Note. For GJ 832 and GJ 667C there is no v sin i measurement. We assumed a v sin i = 3.0 corresponding to the peak of the distribution (Jenkins et al. 2009) when generating a PHOENIX model. See text for references.

model planet corresponds to Earth's current surface of 70% ocean, 2% coast, and 28% land. The land surface consists of 30% grass, 30% trees, 9% granite, 9% basalt, 15% snow, and 7% sand. Surface reflectivities are taken from the USGS Digital Spectral Library[9] and the ASTER Spectral Library[10] (following Kaltenegger et al. 2007).

Clouds have a strong impact on the detectability of atmospheric species. For the spectra shown in Figures 7–9, we assume a 60% global cloud cover with cloud layers analogous to Earth (40% water clouds at 1 km, 40% water clouds at 6 km, and 20% ice clouds at 12 km, following Kaltenegger et al. 2007). In the visible to NIR, clouds increase the reflectivity of an Earth-like planet substantially and therefore increase the equivalent widths of all observable features, even though clouds block access to some of the lower atmosphere. In the IR, clouds slightly decrease the overall emitted flux of an Earth-like planet because they radiate at lower temperatures and therefore decrease the equivalent widths of all observable absorption features, even though they can increase the relative depth of a spectral feature as a result of lowering the continuum temperature of the planet. For a comparison of scenarios with Earth-analog clouds to those of clear sky spectra see Rugheimer et al. (2013).

Using 34 layers, we calculate the spectrum at high spectral resolution with several points per line width. The line shapes and widths are computed using Doppler and pressure broadening on a line-by-line basis for each layer in the model atmosphere. The overall high-resolution spectrum is calculated with 0.1 cm^{-1} wavenumber steps. The figures are shown smoothed to a resolving power of 150 in the IR and 800 in the visible using a triangular smoothing kernel. The spectra may be binned further for comparison with proposed future spectroscopy missions designed to characterize Earth-like planets. We previously validated EXO-P from the visible to the IR using data from ground and space (Kaltenegger et al. 2007; Kaltenegger & Traub 2009; Rugheimer et al. 2013).

2.3. Simulation Setup

To examine the effects of the varying UV flux of M dwarfs on an Earth-like atmosphere and its observable spectral features, we use the temperature grid of stellar models ranging from M9 to M0 ($T_{\rm eff}$ = 3800–2300 K) for active and inactive models, along with the six M dwarfs with well-characterized UV fluxes from *HST* (see Section 2.2). We simulated an Earth-like planet with the same mass as Earth at the 1 AU equivalent orbital distance, defined by the wavelength integrated stellar flux received on top of the planet's atmosphere being equivalent to 1 AU in our solar system, calculated by $1\ {\rm AU_{eq}} = {\rm AU} \times \sqrt{(R/R_\odot)^2 \times (T_{\rm eff}/T_{{\rm eff}\,\odot})^4}$.

The biogenic (produced by living organisms) fluxes were held fixed in the models in accordance with the fluxes that reproduce the modern mixing ratios in the Earth–Sun case, except for the cooler M dwarfs, where CH_4 and N_2O were given a fixed mixing ratio of 1.0×10^{-3} and 1.5×10^{-2}, respectively (following Segura et al. 2003, 2005). The surface fluxes for the long-lived gases H_2, CH_4, N_2O, CO, and CH_3Cl were calculated such that the Earth around the Sun yields a $T_{\rm surf}$ = 288 K for surface mixing ratios: $cH_2 = 5.5 \times 10^{-7}$, $cCH_4 = 1.6 \times 10^{-6}$, $cCO_2 = 3.5 \times 10^{-4}$, $cN_2O = 3.0 \times 10^{-7}$, $cCO = 9.0 \times 10^{-8}$, and $cCH_3Cl = 5.0 \times 10^{-10}$ (see Rugheimer et al. 2013). The corresponding input surface fluxes to the atmosphere are -1.9×10^{12} g H_2 yr^{-1}, 5.3×10^{14} g CH_4 yr^{-1}, 7.9×10^{12} g N_2O yr^{-1}, 1.8×10^{15} g CO yr^{-1}, and 4.3×10^{12} g CH_3Cl yr^{-1}. The N_2 mixing ratio is set to be a "fill gas" such that the total surface pressure is 1 bar. These boundary conditions were used for M0–M5 active grid stars, M0–M3 inactive grid stars, and all MUSCLES stars.

For M6–M9 active grid stars and for M4–M9 inactive grid stars, the boundary condition for CH_4 is changed to a fixed mixing ratio once the UV environment of the host star drops below a certain level because CO, H_2, and CH_4 do not converge according to the criteria described in Section 2.2 assuming a modern Earth biological flux (see also Segura et al. 2005). In reality, the thermodynamical cost for microbes producing CH_4 would become unprofitable as temperatures would initially rise owing to the increased greenhouse effect, causing the microbes to operate less efficiently. This type of biological feedback is not included in the models. CH_4 is produced biotically by methanogens and other organisms and abiotically through hydrothermal vent systems. In the modern atmosphere there is a significant anthropogenic source of CH_4 from natural gas, livestock, and rice paddies. Upper limits of abiotic fluxes of methane can be estimated for terrestrial planets following Guzmán-Marmolejo et al. (2014). An estimate of Earth biotic methane is about 30 times the abiotic flux (see discussion in Segura et al. 2005), and thus a range of methane fluxes may be maintained on a terrestrial planet via methanogenesis in addition to abiotic methane production.

Therefore, we set the mixing ratio of CH_4 to 1×10^{-3}, corresponding to a value of the last stable run with an Earth-like biological CH_4 flux for an active M5 star for planets

[9] http://speclab.cr.usgs.gov/spectral-lib.html
[10] http://speclib.jpl.nasa.gov

around host stars that show this "runaway" behavior. Given these boundary conditions, the methane flux necessary to sustain a 1×10^{-3} mixing ratio of methane is 5.65×10^{14} g yr^{-1} (equal to our present Earth methane flux) for the planet around the hottest M dwarf ($T_{\rm eff} = 3800$ K), either active or inactive, 1.16×10^{14} g yr^{-1} (20.5% of the Earth value) for the planet around the coolest ($T_{\rm eff} = 2300$ K) active star, and 5.87×10^{12} g yr^{-1} (1% of the Earth value) for the coolest inactive M dwarf of our sample.

For the less active stars, we set the deposition velocity (rate at which they are deposited to the surface) for H_2 and CO to 2.4×10^{-4} cm s^{-1} and 1.2×10^{-4} cm s^{-1}, respectively (see also Kharecha et al. 2005; Segura et al. 2005). Rauer et al. (2011) used a deposition velocity for H_2 of 7.7×10^{-4} cm s^{-1}. This number was obtained after calibrating the model to reproduce the H_2 atmospheric abundance measured for present Earth. In our case, the deposition values for H_2 and CO correspond to maximum air–sea transfer rates estimated using the "piston velocity" approach (Broecker 1982; Kharecha et al. 2005). Since a larger H_2 deposition velocity implies consumption by bacteria, we use the abiological value in Kharecha et al. (2005).

We followed a similar procedure for constraining the N_2O concentrations for M6–M9 inactive stars. We set the mixing ratio of N_2O to 1.5×10^{-2}, corresponding to values of the last stable run with Earth-like biological fluxes, to prevent unphysical buildup of N_2O. N_2O is emitted primarily by (de) nitrifying bacteria with anthropogenic sources from fertilizers in agriculture, biomass burning, industry, and livestock and is a relatively minor constituent of the modern atmosphere at around 320 parts per billion (ppb), compared to the preindustrial concentration of 270 ppb (Forster et al. 2007).

We used modern Earth fluxes for all of the MUSCLES stars without any "runaway" buildup of reduced gases. The CH_4 and N_2O fluxes are given in Table 3.

All of our simulations used a fixed mixing ratio of 355 ppm for CO_2, 21% O_2, and a fixed upper boundary of 10^{-4} bar (~60 km). In the 1D climate model, a surface albedo of 0.2 is fixed for all simulations, corresponding to the surface albedo that reproduces Earth's average temperature of 288 K for the Earth/Sun case. The planetary Bond albedo (surface + atmosphere) is calculated by the 1D climate code.

3. ATMOSPHERIC MODEL RESULTS

The amount of UV radiation emitted from the host star influences the abundances of major chemical atmospheric constituents, including H_2O, CH_4, and O_3, and, as a result, modifies the temperature-pressure profile of a planet. The UV fluxes incident at the top of the atmosphere of an Earth-like planet in the habitable zone are given in Table 4 and shown in Figure 3. An M0 active star model has 6.7 times more total UV flux than an M0 inactive star model. An M9 active star model has 4600 times more total UV flux than an M9 inactive star model. The greatest differences are in the FUV (1000–2000 Å), where an active star model has 6.8×10^4 and 1.3×10^{11} more FUV flux than an inactive M0 and M9 model, respectively. The MUSCLES stars' UV environments fall between the active and inactive star models, consistent with their classification as being weakly active.

The temperature versus altitude profile and the H_2O, O_3, CH_4, and N_2O mixing ratio profiles for all of the simulations are shown in Figure 4, with each row corresponding to active, inactive, and MUSCLES star models, respectively. CH_3Cl profiles are not shown here, but follow the same trends as CH_4. Since both O_2 and CO_2 are well mixed in the atmosphere, their vertical mixing ratio profiles of 0.21 and 355 ppm, respectively, are not shown.

In the first column of Figure 4, we show the changes in the temperature/altitude profile for Earth-like atmosphere models around M dwarfs for active (top row), inactive (middle row), and the six observed MUSCLES stars (bottom row). All temperature inversions are weaker than for the modern Earth because M dwarfs emit low UV flux in the 2000–3000 Å wavelength region, thereby producing near-isothermal stratospheres (see also Segura et al. 2005). Figure 4 shows that temperature inversions are weaker for the higher UV environment stars. This is counterintuitive since for the modern Earth, O_3 absorption of UV radiation causes stratospheric heating and an inversion. However, in these lower UV environments, additional heating is provided by stratospheric CH_4 and H_2O.

H_2O concentrations are lower in the stratosphere for planets around M dwarf models with higher UV fluxes, although higher O_3 concentrations will act as a shield, partially offsetting the effect of higher UV photon fluxes (Figure 4, second column). H_2O can also be formed in the stratosphere from CH_4 and OH ($CH_4 + OH \rightarrow CH_3 + H_2O$) and by increased upward vertical transport in the nearly isothermal stratospheres of Earth-like planets orbiting M dwarfs (see also Segura et al. 2005). O_3 shields H_2O in the troposphere from UV environments. While photochemically inert in the troposphere, H_2O can be removed by photolysis at wavelengths shortward of 2000 Å in the stratosphere (see columns 2 and 3 in Table 4) or by reactions with excited oxygen, $O(^1D)$, to produce OH radicals.

In an atmosphere containing O_2, O_3 concentrations are determined primarily by the absorption of UV light shortward of 2400 Å in the stratosphere, and we see a corresponding decrease in O_3 concentrations correlated with decreased FUV radiation for cooler M dwarfs, as well as inactive versus active stars (Figure 4, third column).

CH_4 mixing ratio profiles are shown in column 4 of Figure 4. As mentioned previously, we set the mixing ratio of methane to be 1000 ppm for the later M dwarf spectral types as described in Section 2.3 and Table 3. For Earth-like CH_4 fluxes, CH_4 concentrations decrease with higher UV environments owing to reactions with OH to form H_2O and by photolysis by $\lambda < 1500$ Å (Figure 4, fourth column).

N_2O mixing ratios are larger for cooler M dwarfs because cooler stars have smaller UV fluxes at $\lambda < 2200$ Å and thus lower photolysis rates. Around later M dwarfs, we see mixing ratios of N_2O that increase unrealistically for the inactive stellar models M6–M9, similar to CH_4 (Figure 4, fifth column). Since such a "runaway" effect should not be sustainable by biology, we cap the N_2O to a fixed mixing ratio corresponding to the last stable run for the inactive model M5. N_2O is also an indirect sink for stratospheric O_3, since about 1% is converted to NO. Therefore, increasing N_2O decreases O_3 abundance.

OH concentrations decrease with decreasing UV levels (in cooler and inactive M dwarfs), and OH is a primary sink for many species in the atmosphere, including, but not limited to, many biologically interesting species such as CH_4, CH_3, HCl, H_2, H_2S, and CH_3Cl. CH_3Cl concentrations increase for cooler and inactive M dwarfs owing to decreased stellar UV flux.

Table 3
CH_4 and N_2O Fluxes and Mixing Ratios and O_3 Column Depths

	Surface Mixing Ratio CH_4	Flux (g yr^{-1}) CH_4	% Earth CH_4 flux	Surface Mixing Ratio N_2O	Flux (g yr^{-1}) N_2O	% Earth N_2O flux	O_3 Column Depth (cm^{-2})
			Active				
M0 A	330 ppm	5.65×10^{14}	100%	0.70 ppm	7.99×10^{12}	100%	4.1×10^{18}
M1 A	370 ppm	5.65×10^{14}	100%	0.70 ppm	7.99×10^{12}	100%	4.0×10^{18}
M2 A	450 ppm	5.65×10^{14}	100%	0.76 ppm	7.99×10^{12}	100%	3.8×10^{18}
M3 A	570 ppm	5.65×10^{14}	100%	0.82 ppm	7.99×10^{12}	100%	3.6×10^{18}
M4 A	910 ppm	5.65×10^{14}	100%	0.93 ppm	7.99×10^{12}	100%	3.5×10^{18}
M5 A	1000 ppm	5.65×10^{14}	100%	0.98 ppm	7.99×10^{12}	100%	2.6×10^{18}
M6 A	1000 ppm	2.90×10^{14}	51.8%	1.7 ppm	7.99×10^{12}	100%	3.1×10^{18}
M7 A	1000 ppm	1.28×10^{14}	22.7%	3.0 ppm	7.99×10^{12}	100%	2.4×10^{18}
M8 A	1000 ppm	1.36×10^{14}	24.0%	3.1 ppm	7.99×10^{12}	100%	2.5×10^{18}
M9 A	1000 ppm	1.20×10^{14}	21.2%	3.5 ppm	7.99×10^{12}	100%	2.3×10^{18}
			Inactive				
M0 I	490 ppm	5.65×10^{14}	100%	34 ppm	7.99×10^{12}	100%	1.7×10^{18}
M1 I	580 ppm	5.65×10^{14}	100%	64 ppm	7.99×10^{12}	100%	1.5×10^{18}
M2 I	650 ppm	5.65×10^{14}	100%	120 ppm	7.99×10^{12}	100%	1.4×10^{18}
M3 I	1000 ppm	5.65×10^{14}	100%	360 ppm	7.99×10^{12}	100%	1.3×10^{18}
M4 I	1000 ppm	4.15×10^{14}	73.5%	670 ppm	7.99×10^{12}	100%	1.0×10^{18}
M5 I	1000 ppm	1.23×10^{14}	21.8%	15000 ppm	7.99×10^{12}	100%	4.5×10^{17}
M6 I	1000 ppm	2.42×10^{13}	4.3%	15000 ppm	4.04×10^{11}	5.1%	1.4×10^{17}
M7 I	1000 ppm	1.67×10^{13}	3.0%	15000 ppm	4.96×10^{10}	0.6%	6.1×10^{16}
M8 I	1000 ppm	1.34×10^{13}	2.4%	15000 ppm	5.72×10^{9}	0.07%	2.6×10^{16}
M9 I	1000 ppm	5.87×10^{12}	1.0%	15000 ppm	3.17×10^{9}	0.04%	1.1×10^{16}
			MUSCLES				
GJ 832	550 ppm	5.65×10^{14}	100%	15 ppm	7.99×10^{12}	100%	1.6×10^{18}
GJ 667C	330 ppm	5.65×10^{14}	100%	0.7 ppm	7.99×10^{12}	100%	7.0×10^{18}
GJ 1214	1600 ppm	5.65×10^{14}	100%	1.1 ppm	7.99×10^{12}	100%	2.3×10^{18}
GJ 436	1600 ppm	5.65×10^{14}	100%	4.3 ppm	7.99×10^{12}	100%	1.1×10^{18}
GJ 581	1400 ppm	5.65×10^{14}	100%	2.9 ppm	7.99×10^{12}	100%	1.2×10^{18}
GJ 876	3400 ppm	5.65×10^{14}	100%	6.9 ppm	7.99×10^{12}	100%	8.8×10^{17}

O_2 and CO_2 concentrations remain constant and well mixed for all stellar types.

The planetary surface temperatures range between 297 and 304 K and Bond albedos range between 0.108 and 0.06 for M0 to M9 stars, respectively (see Figure 5). These albedos are lower than Earth's Bond albedo of 0.3 around the Sun because the stellar SEDs peak at longer wavelengths for cooler stars, where Rayleigh scattering is less efficient, assuming the same total insolation.

3.1. Effect of Lyα

Lyα is the brightest line in the UV spectra for cool stars and accounts for a significant portion of the overall UV flux. However, the intrinsic Lyα flux must be reconstructed to account for interstellar absorption by neutral hydrogen (see Wood et al. 2005; Linsky et al. 2013). For the observed MUSCLES stars, the Lyα line flux is 13%–33% the total UV flux excluding Lyα. GJ 1214 has no observed Lyα and only an upper limit that is 0.5% of the total UV flux (France et al. 2013). In our active models, Lyα ranges from 2% to 17% of the total UV flux based on observations of AD Leo. In the inactive models (i.e., no chromosphere) Lyα is negligible compared with total UV flux.

We ran two sensitivity tests of the photochemistry of Earth-like planets to the amount of Lyα flux from their host star. First, we increased the Lyα by a factor of 10^3, 10^6, 10^9, 10^{12}, and 10^{15} above the M0 inactive model, corresponding to flux levels of 2.7×10^{-8}, 2.7×10^{-5}, 2.7×10^{-2}, 2.7×10^{1}, 2.7×10^{4} ergs cm^{-2} s^{-1}, respectively. The highest Lyα value considered is 84× higher than that of the M0 active model and 180× higher than the highest observed Lyα flux in the MUSCLES stellar sample. As seen in Figure 6 (top), increasing the Lyα flux has only a small effect on the photochemistry until the most extreme case considered, where it primarily photolyzes N_2O and CH_4. We run our models to around 60 km, corresponding to a pressure of 1×10^{-4} bars. The effect of Lyα will be more pronounced at pressures lower than this, as Miguel et al. (2015) has shown for mini-Neptune atmospheres.

GJ 1214 is the only MUSCLES star to not have a directly detected Lyα flux. An upper limit was placed at 2.4×10^{-15} ergs cm^{-2} s^{-1}. We artificially set the Lyα flux to be 10^{-2}, 10^{-1}, 10^{1}, 10^{2}, and 10^{3} times this upper limit. We tested values both above and below the upper limit to see how sensitive an Earth-like planet atmosphere is to changes in Lyα flux when the rest of the NUV radiation field is still much higher than the inactive model in the previous sensitivity test. As shown in Figure 6 (bottom), the largest changes are seen in the CH_4 and to a

Table 4
Integrated UV Fluxes at the Top of the Atmosphere

Stellar Type	Lyα TOA 1210–1222 Å (ergs cm^{-2} s^{-1})	FUV minus Lyα TOA 1222–2000 Å (ergs cm^{-2} s^{-1})	FUV TOA 1000–2000 Å (ergs cm^{-2} s^{-1})	NUV TOA 2000–3200 Å (ergs cm^{-2} s^{-1})	Full UV TOA 1000–3200 Å (ergs cm^{-2} s^{-1})
			Active		
M0 A	6.9×10^{2}	2.4×10^{2}	9.4×10^{2}	1.4×10^{3}	2.3×10^{3}
M1 A	5.6×10^{2}	2.0×10^{2}	7.6×10^{2}	1.1×10^{3}	1.9×10^{3}
M2 A	4.4×10^{2}	1.6×10^{2}	6.1×10^{2}	8.5×10^{2}	1.5×10^{3}
M3 A	3.5×10^{2}	1.2×10^{2}	4.7×10^{2}	6.5×10^{2}	1.1×10^{3}
M4 A	3.1×10^{2}	1.1×10^{2}	4.2×10^{2}	5.6×10^{2}	9.8×10^{2}
M5 A	1.8×10^{2}	6.3×10^{1}	2.5×10^{2}	3.3×10^{2}	5.8×10^{2}
M6 A	6.4×10^{1}	2.3×10^{1}	8.8×10^{1}	1.2×10^{2}	2.1×10^{2}
M7 A	2.6×10^{1}	9.2×10^{0}	3.6×10^{1}	4.8×10^{2}	8.4×10^{2}
M8 A	2.6×10^{1}	9.0×10^{0}	3.5×10^{1}	4.7×10^{2}	8.2×10^{2}
M9 A	2.2×10^{1}	7.6×10^{0}	3.0×10^{1}	3.9×10^{2}	6.9×10^{2}
			Inactive		
M0 I	2.7×10^{-11}	9.4×10^{-3}	9.5×10^{-3}	3.0×10^{2}	3.0×10^{2}
M1 I	5.8×10^{-12}	2.9×10^{-3}	2.9×10^{-3}	2.6×10^{2}	2.6×10^{2}
M2 I	1.5×10^{-12}	9.1×10^{-4}	9.1×10^{-4}	1.7×10^{2}	1.7×10^{2}
M3 I	3.5×10^{-14}	6.9×10^{-5}	6.9×10^{-5}	8.9×10^{1}	8.9×10^{1}
M4 I	6.1×10^{-15}	2.2×10^{-5}	2.2×10^{-5}	5.9×10^{1}	5.9×10^{1}
M5 I	2.9×10^{-19}	1.5×10^{-8}	1.5×10^{-8}	1.3×10^{1}	1.3×10^{1}
M6 I	4.2×10^{-21}	2.6×10^{-9}	2.6×10^{-9}	3.0×10^{0}	3.0×10^{0}
M7 I	1.1×10^{-21}	2.6×10^{-10}	2.6×10^{-10}	1.3×10^{0}	1.3×10^{0}
M8 I	8.3×10^{-24}	1.7×10^{-10}	1.7×10^{-10}	5.0×10^{-1}	5.0×10^{-1}
M9 I	1.8×10^{-24}	1.6×10^{-10}	1.6×10^{-10}	1.3×10^{-1}	1.3×10^{-1}
			MUSCLES		
GJ 832	1.5×10^{2}	3.0×10^{0}	1.5×10^{2}	3.5×10^{2}	5.0×10^{2}
GJ 667C	1.2×10^{2}	2.4×10^{0}	1.3×10^{2}	2.3×10^{2}	3.6×10^{2}
GJ 1214	1.4×10^{0}	9.9×10^{1}	1.1×10^{2}	1.8×10^{2}	2.8×10^{2}
GJ 436	6.1×10^{1}	7.1×10^{0}	6.8×10^{1}	2.3×10^{2}	2.9×10^{2}
GJ 581	4.2×10^{1}	6.8×10^{0}	5.0×10^{1}	2.7×10^{2}	3.2×10^{2}
GJ 876	3.4×10^{1}	1.1×10^{1}	4.9×10^{1}	1.1×10^{2}	1.6×10^{2}

smaller extent in stratospheric H_2O concentrations. O_3 and N_2O remain relatively constant through the five order of magnitude change in Lyα flux.

Figures 4 and 6 show that it is important to characterize the entire UV spectrum, including the NUV and the base level flux between emission lines, to understand future observations of extrasolar planet atmospheres. Lyα is one of the most important lines to characterize.

4. RESULTS: SPECTRA OF EARTH-LIKE PLANETS ORBITING M DWARFS

Spectra of Earth-like planets orbiting M dwarfs with varying UV activity levels show measureable differences in spectral feature depths. In the visible, the depth of absorption features is primarily sensitive to the abundance of the species, while in the IR, both the abundance and the temperature difference between the emitting/absorbing layer and the continuum influence the depth of features.

We assume full phase (secondary eclipse) for all spectra presented to show the maximum flux that can be observed. Figures 7–12 show an Earth-size planet to determine the specific flux and planet-to-star contrast ratio. A super-Earth with up to twice Earth's radius will provide 4 times more flux and a better contrast ratio. No noise has been added to these model planetary spectra to provide inputs for a wide variety of instrument simulators for both secondary eclipse and direct detection missions.

4.1. Earth-like Visible/NIR Spectra (0.4–4 μm)

Figure 7 shows the reflected visible and NIR spectra from 0.4 to 2 μm of Earth-like planets around the M dwarf grid of active, inactive, and MUSCLES stars, using the SED of the host star. We assume Earth-analog cloud cover. The high-resolution spectra calculated with 0.1 cm^{-1} steps have been smoothed to a resolving power of 800 using a triangular smoothing kernel to show the individual features more clearly. The Earth–Sun spectrum is shown for comparison as a dashed black line.

Owing to the increased stellar flux at shorter wavelengths for a G-type star, Rayleigh scattering is much more pronounced for FGK stars, which greatly increases the flux from 0.4 to 0.8 μm for an Earth-like planet around a hotter star. Since M dwarfs have stronger NIR emission, the 1–2 μm flux is larger around Earth-like planets orbiting M dwarfs than for the Earth–Sun equivalent. The most notable features in the visible/NIR spectra are O_3 at 0.6 μm (the Chappuis band), O_2 at 0.76 μm, H_2O at 0.95 μm, and CH_4 at 0.6, 0.7, 0.8, 0.9, 1.0, and 1.7 μm. Note that shallow spectral features like the visible O_3 feature would require a very high signal-to-noise ratio (S/N) to be detected.

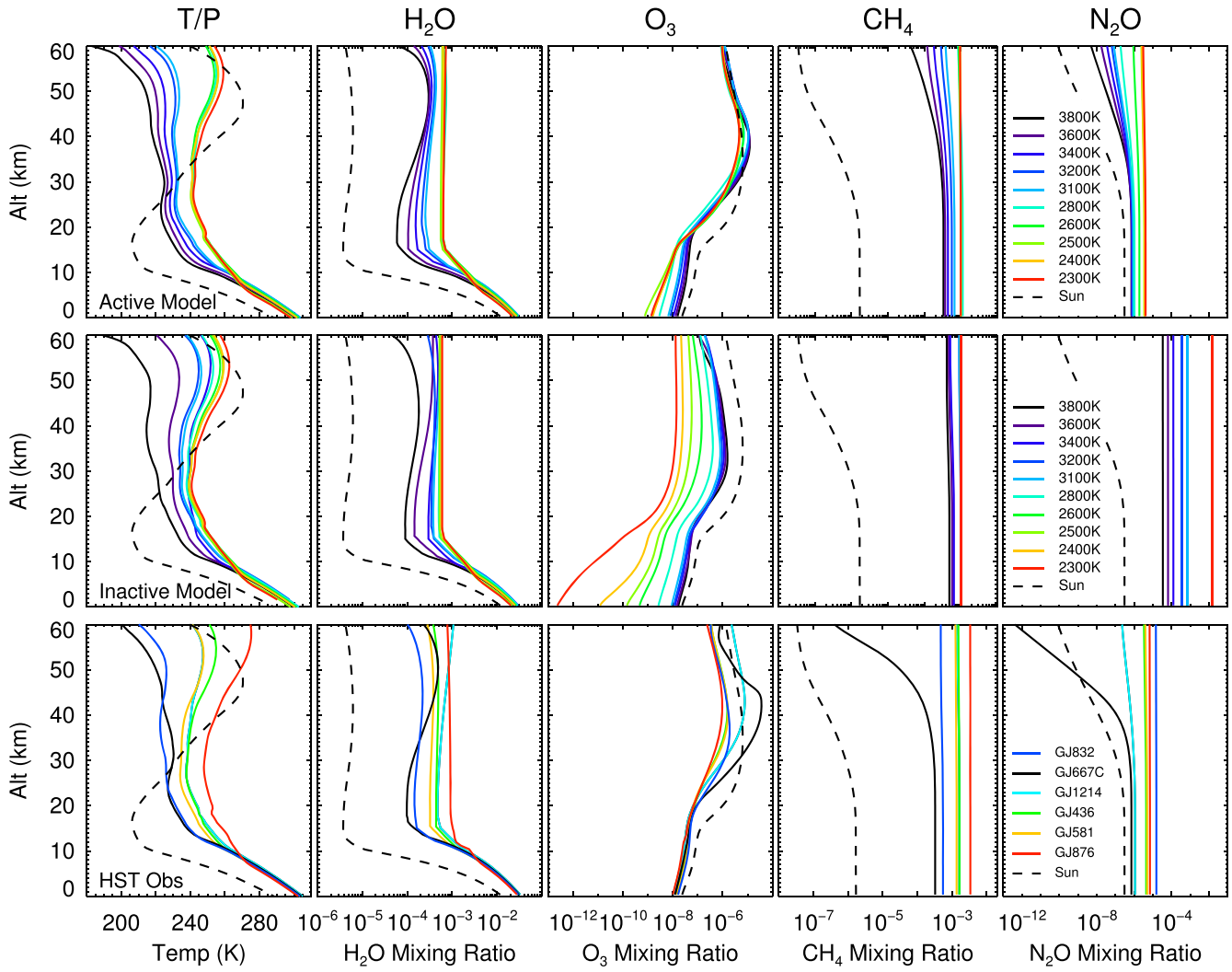


Figure 4. Planetary temperature vs. altitude profiles and mixing ratio profiles profiles for H_2O, O_3, CH_4, and N_2O (left to right) for an Earth-like planet orbiting the grid of active stellar models (top), inactive stellar models (middle), and MUSCLES stars (bottom). Earth–Sun profiles are shown for comparison (dashed black lines).

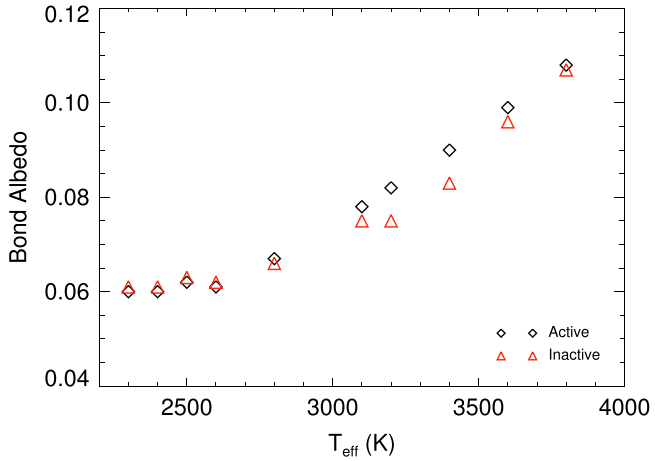


Figure 5. Calculated Bond albedos for Earth-like planets orbiting the M0–M9 active (black diamond) and inactive (red triangle) stellar models.

Figure 8 shows details for one of the most notable feature in the visible, the O_2 A band at 0.76 μm in both the relative flux as planet-to-star contrast ratio (left) and the reflected emergent flux for a 60% cloud cover model for M0–M9 model stars (top middle) and for the six MUSCLES stars (top right). Note that the detectability of the O_2 feature in reflected light is similar for active and inactive models since the stellar flux at 0.76 μm is activity independent. The relative flux shows an equivalently deep feature for each case owing to a constant mixing ratio of 21%. However, the oxygen feature in absolute flux (Figure 8, upper middle panel) becomes increasingly difficult to detect for the later stellar types. For the latest M stellar types modeled here, the detection of the O_2 feature requires a very high S/N to detect even if the planet has an active photosynthetic biosphere like Earth (see Figure 7). If one assumes a blackbody radiation Planck function, rather than a realistic stellar model, when calculating the shape of the reflected light curve, the reduction in the feature's depth on moving to later stellar types (i.e., going from blue to red lines in Figure 8, second and third columns) is less pronounced. The O_2 feature is pronounced for all MUSCLES stars since none of those stars have a low enough $T_{\rm eff}$ for the O_2 feature to be diminished by the SED. GJ 876 is the coolest MUSCLES star, with $T_{\rm eff} = 3129$ K, and in our models the O_2 feature becomes most obscured for stars with $T_{\rm eff} = 2300$–2600 K.

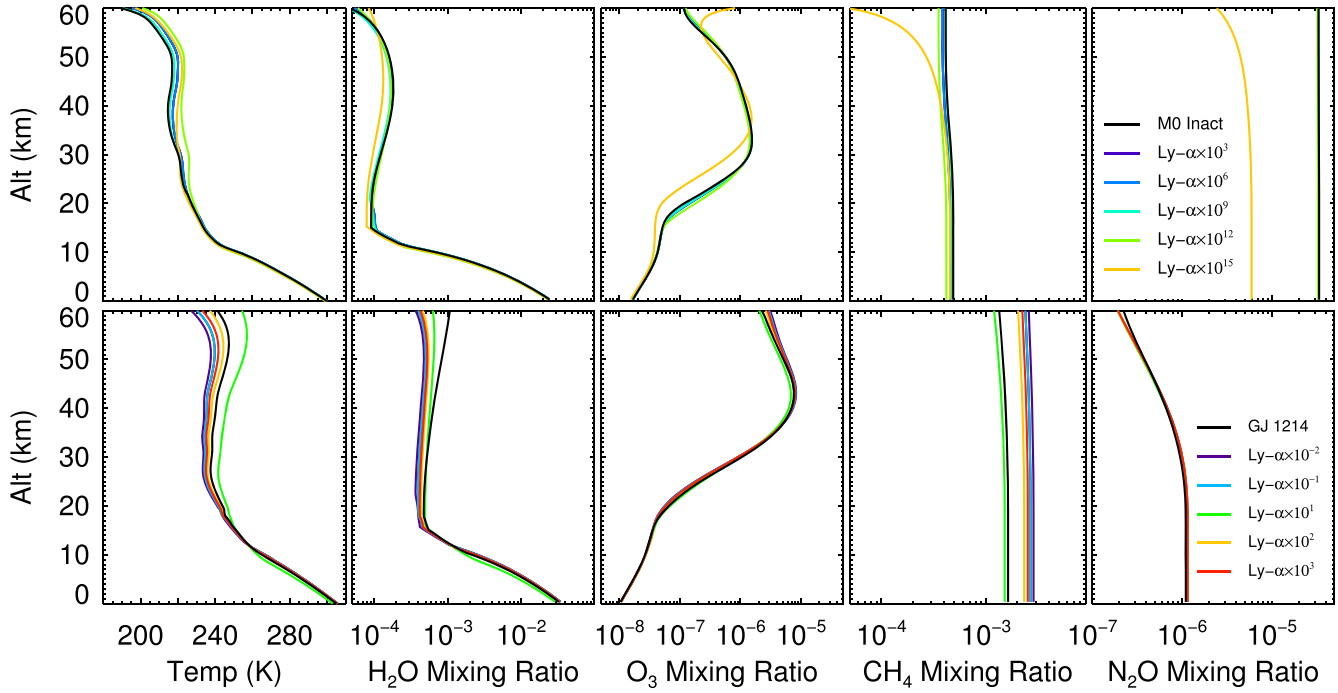


Figure 6. Temperature and H_2O, O_3, CH_4, and N_2O mixing ratio profiles where the Lyα has been increased by a factor of 10^3, 10^6, 10^9, 10^{12}, and 10^{15} above the inactive M0 model star, corresponding to flux levels of 2.7×10^{-8}, 2.7×10^{-5}, 2.7×10^{-2}, 2.7×10^{1}, and 2.7×10^{4} ergs cm^{-2} s^{-1}, respectively (top), and for GJ 1214, where the Lyα upper limit (2.4×10^{-15} ergs cm^{-2} s^{-1}) has been multiplied by a factor of 10^{-2}, 10^{-1}, 10^{1}, 10^{2}, and 10^{3} (bottom).

CH_4 also has several features of interest in the visible/NIR range at 0.6, 0.7, 0.8, 0.9, 1.0, and 1.7 μm (see Figure 9). The CH_4 feature is deeper for less active and cooler M dwarfs. In particular, the CH_4 features at 0.8, 0.9, and 1.0 μm become much more pronounced for the cooler M dwarfs and for some of the MUSCLES stars, such as GJ 876.

H_2O has several features in the visible/NIR at 0.95, 1.14, 1.41, 1.86 μm. These features are deeper for cooler and less active stars.

Clouds increase reflectivity but can also decrease the depth of all observable features compared to the clear sky case. It will be difficult, therefore, to remotely determine the absolute abundance of a molecule without a well-characterized temperature versus pressure distribution and cloud profile.

4.2. Earth-like Infrared Spectra, IR (4–20 μm)

Figure 10 shows the thermal emission spectra from 4 to 20 μm of Earth-like planets with Earth-analog cloud cover around the M dwarf grid of active, inactive, and MUSCLES stars using the stellar SED. The high-resolution spectra have been smoothed to a resolving power of 150 using a triangular smoothing kernel to show the resolution expected by *JWST*. The Earth–Sun IR spectrum is shown for comparison as a dashed black line. Figure 11 shows the individual component gas contributions of the dominant gases (H_2O, CH_4, CO_2, CH_3Cl, O_3, and N_2O) to the final IR planetary spectrum for an M9 active and inactive stellar model.

The depth of the O_3 feature at 9.6 μm decreases for planets orbiting cooler and less active M dwarfs, as expected owing to lower O_3 abundances for lower UV incident flux and also to the decreased temperature difference between the O_3-emitting layer (around 40 km) and the surface temperature, which is larger for the earlier M dwarfs, as seen in Figure 4.

The CH_4 feature at 7.7 μm decreases in depth for planets orbiting cooler M dwarfs, despite increasing CH_4 abundances making it difficult to remotely determine the CH_4 abundance without a well-characterized temperature versus pressure profile. Note that the 7.7 μm feature is partially obscured by the wings of the H_2O feature at 5–8 μm.

The N_2O features are the most striking addition in the inactive models with low UV flux. N_2O has features at 7.75 (overlapping with the CH_4 feature), 8.5, 10.65, and 16.9 μm (see Figure 11) that become deeper with decreasing UV flux. In the active M0–M9 stellar models we do not see any strong N_2O features, although it does contribute to the depth of the 7.7 CH_4 feature. For the inactive M5–M9 models we see a strong N_2O feature at 10.65 μm and wide absorption from 14–19 μm owing to the strong buildup of N_2O in low UV environments assuming an Earth-like biological surface flux of 7.99×10^{12} g yr^{-1} (see Sections 2 and 3). However, even for modest mixing ratios of 15–34 ppm in GJ 832 and the M0 inactive models, respectively, we see a strong N_2O feature at 16.9 μm. These concentrations are not much higher than the model mixing ratios calculated for the other MUSCLES stars and the later active M dwarf models. N_2O has been considered to be a strong biosignature (see, e.g., Segura et al. 2005; Seager et al. 2012) and will be easier to detect around M dwarfs—especially inactive ones—than around FGK stars.

The CO_2 absorption feature at 15 μm does not have a central emission peak, usually seen in F and G stars, owing to the more isothermal stratospheres of planets around all M dwarfs.

The depth of the H_2O feature at 5–8 μm decreases for later M dwarfs despite increasing stratospheric H_2O concentrations.

Clouds reduce the continuum level and the depth of all of the observable features compared to the clear sky case. Therefore, it will be difficult to remotely determine absolute abundances

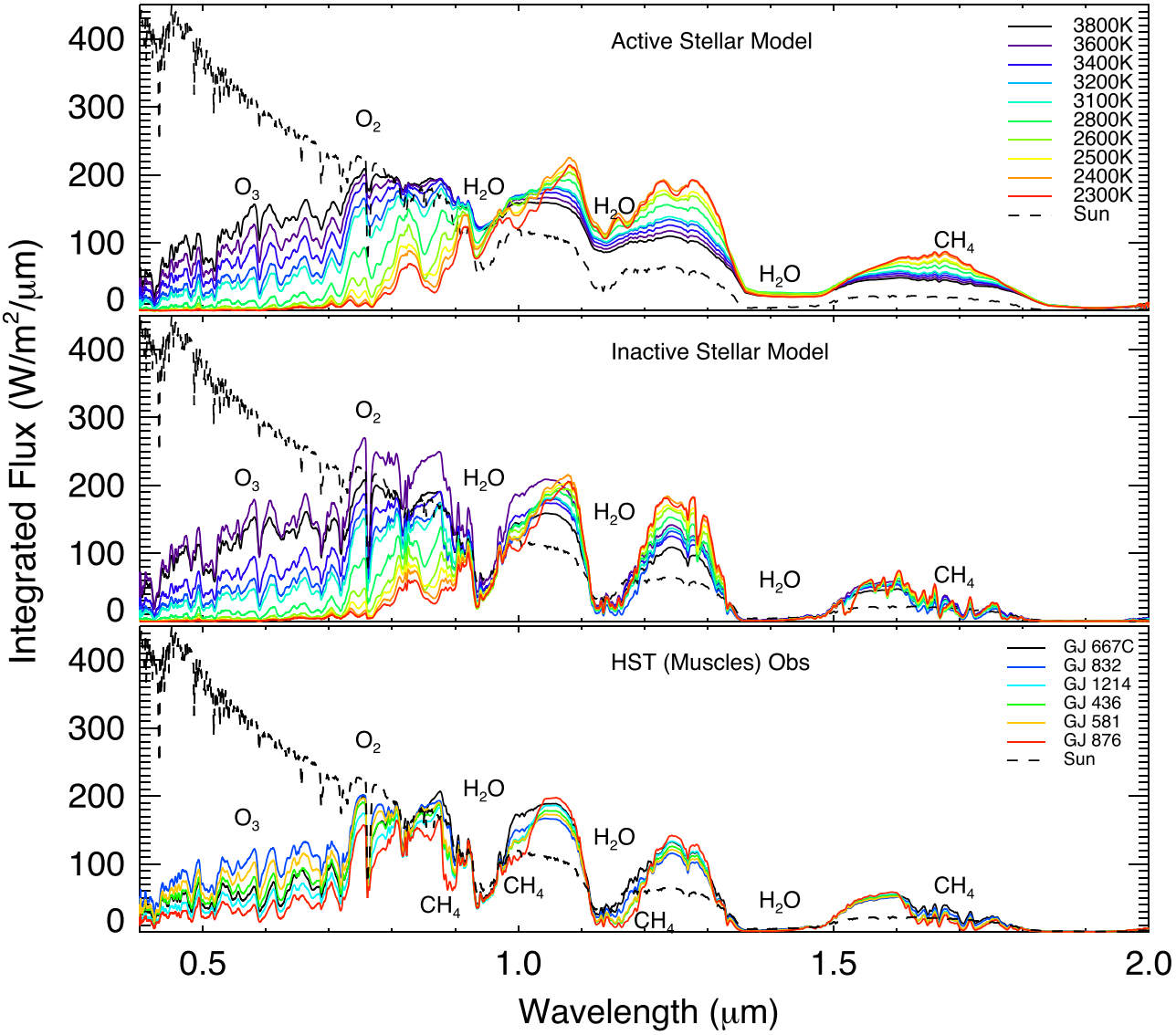


Figure 7. Smoothed, disk-integrated visible/NIR spectra at the TOA for an Earth-like planet for the grid of active stellar models (top), inactive stellar models (middle), and MUSCLES stars (bottom) assuming 60% Earth-analog cloud coverage model (region 2–4 μm has low integrated flux levels and therefore is not shown here). The Earth–Sun spectrum is shown for comparison as a dashed black line.

without a well-characterized temperature versus pressure distribution and cloud profile.

Observability of Biosignatures: detecting the combination of O_2 or O_3 and a reducing gas like CH_4 in emergent spectra and in secondary eclipse measurements requires either observations in the IR between 7 and 10 μm that include the 7.7 μm CH_4 and 9.6 μm O_3 features, or observations in the visible to NIR between 0.7 and 3 μm that include the 0.76 μm O_2 and 2.4 μm CH_4 features in the observed spectral range. The strengths of absorption features (see Figures 7 and 11 for visible/NIR and IR, respectively) depend on the effective temperature of the host star and its UV flux and vary significantly between stellar types (see Figures 7–11).

In the IR, CH_4 at 7.7 μm is more easily detected at low resolution for earlier grid stars (M0–M4) than for later grid stars (M5–M9) in the active models.

The 9.6 μm O_3 feature is deepest in earlier and/or more active M dwarfs, where there are more UV photons. For M5–M9 inactive models, O_3 is not detectable in low resolution at 9.6 μm owing to the extremely low UV flux for these models. The narrow O_2 feature in the visible at 0.72 μm becomes weaker for cooler M dwarfs even though the mixing ratio of O_2 remains fixed in our simulations at 21%. This is a consequence of the faint SEDs at shorter wavelengths for both active and inactive late M stellar models.

For the modern Earth, N_2O and CH_3Cl do not contribute substantially to the spectrum owing to their low mixing ratios and will likely be undetectable by the first low-resolution and photon-limited exoplanet atmosphere characterization missions (Selsis 2000; Kaltenegger et al. 2007). However, both N_2O and CH_3Cl reach detectable levels in the IR spectra for our models of cooler and less active stars owing to low photolysis rates, even though N_2O has many absorption features in the IR (see Figure 11).

N_2O is considered a strong biosignature because there are no significant abiotic sources (Des Marais et al. 2002). One MUSCLES star, GJ 832, has a noticeable N_2O feature at 17 μm, with 15 ppm for a modern Earth-like flux. This case is

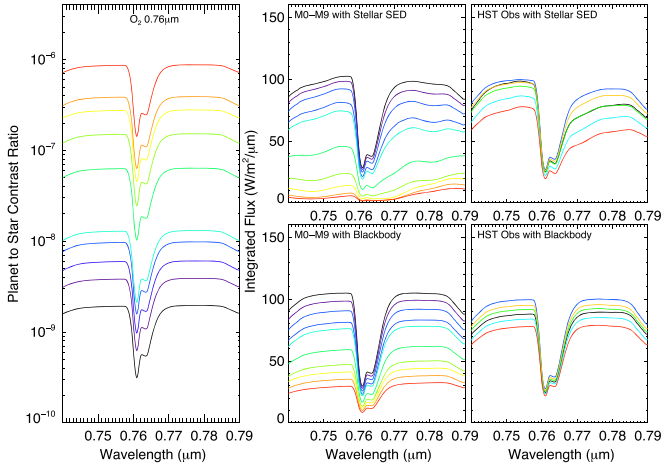


Figure 8. O_2 feature at 0.76 μm relative flux as planet-to-star contrast ratio (left), and the reflected emergent flux for a 60% cloud cover model for M0–M9 model stars (top middle) and for MUSCLES stars (top right). Bottom row shows the same but with a blackbody used to calculate the absolute flux. The observable O_2 feature becomes increasingly difficult to detect for later stellar types owing to the decreasing stellar flux in this wavelength region. Coloring is the same as in Figure 7.

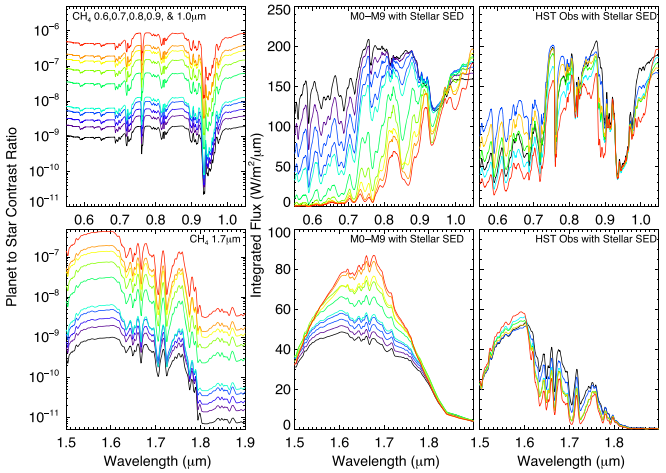


Figure 9. CH_4 features at 0.6, 0.7, 0.8, 0.9, and 1.0 μm (top row) and the CH_4 feature at 1.7 μm (bottom row) for the relative flux as planet-to-star contrast ratio (left) and the reflected emergent flux for a 60% cloud cover model for M0–M9 model stars (middle) and for MUSCLES stars (right). The observable CH_4 feature becomes deeper for planets orbiting cooler and less active star models. Coloring is the same as in Figure 7.

interesting because GJ 832 has the highest total FUV flux at wavelengths where N_2O is photolyzed (1000–2400 Å). We find that the high Lyα flux of GJ 832 promotes the destruction of O_3, producing more $O(^1D)$, which then reacts with N_2 to form N_2O.

For planets orbiting inactive M5–M9 star models we observe a sharp increase in N_2O concentrations as a consequence of few available UV photons. N_2O features dominate the spectrum for these late, inactive M dwarfs and can be detected in the IR at 4–5 μm, 8–11 μm, and 16–19 μm (see Figure 11). In an atmosphere dominated by N_2O, such strong absorption throughout the IR could obscure the 7.7 μm CH_4 feature. It is unknown whether a strong buildup of biotic N_2O would be physically possible around stars with little or no chromospheric flux. Given the existence of a few *GALEX* stars with little excess chromospheric NUV flux (Shkolnik & Barman 2014) and only an upper limit established for the Lyα flux from GJ 1214, a small fraction of M dwarfs could exhibit low UV fluxes. However, the MUSCLES data set shows that all six observed M dwarfs have sufficient UV flux to photolyze N_2O and to prevent "runaway" N_2O buildup.

CH_3Cl contributes to our IR spectrum from 13 to 14 μm in the short-wavelength wing of the CO_2 and N_2O features and could also be detectable, depending on the CO_2 and N_2O concentrations present (see Figure 11).

For clear sky models, the vegetation red edge (VRE) surface feature is detectable in low-resolution spectra owing to the order-of-magnitude-increased VRE reflectance between 0.7 and 0.75 μm for all M grid stars assuming that the exoplanets of these host stars have similar plant life (see Rugheimer et al. 2013 for FGK stars). Clouds partly obscure this feature compared to the clear sky case, although the increase in flux can be seen at 0.7 μm in Figure 7, which includes Earth-like clouds. Owing to the shift in available photons to longer wavelengths for M dwarfs, a different photosynthesis biochemistry could have evolved, resulting in a different but potentially observable vegetation signature (Kiang et al. 2007).

Observability of Spectral Features: note that we have not added noise to these model spectra in order to be useful as input models for a wide variety of instrument simulators for both secondary eclipse and direct detection simulations. Different instrument simulators for *JWST* (see, e.g., Deming et al. 2009; Kaltenegger & Traub 2009) explore the capability of *JWST*'s MIRI and NIRspec instruments to characterize extrasolar Earth-like planets for nearby and luminous host stars. Several groups are providing realistic instrument simulators that can be used to determine the detectability of these absorption features. Future ground- and space-based telescopes are being designed to characterize exoplanets as small as Earth-like planets and will provide opportunities to observe atmospheric features, especially for super-Earths with radii up to twice Earth's radius and therefore four times the flux and planet-to-star contrast ratio levels for Earth-size planets, as shown in Figure 12.

In addition to measuring the size of the planet, future observations will occur at different phases throughout the planet's orbit. The maximum observable planetary flux in the visible spectrum scales with the illuminated fraction of the planet that is visible to the observer. At quadrature, representing an average viewing geometry, the contrast ratios presented in Figure 12 will be a factor of ~2 lower in the visible. In the IR, the maximum flux remains constant throughout the planet's orbit, assuming a similar temperature on the planet's dayside and nightside.

5. DISCUSSION

Our active and inactive stellar models represent the extreme ends of stellar activity for M dwarfs. AD Leo, our active star proxy with Hα in emission, was chosen to represent a young, active star. Our inactive stellar models assume no chromospheric activity, which is the lowest level possible of UV flux. More observations are needed to determine the lowest possible level of UV flux around an M dwarf, which still might be significantly higher than the photosphere-only models. Many M dwarfs exhibit a wide range of activity. Therefore, we use the MUSCLES star database to represent observed M dwarfs with a range of activity between the two extremes. The simulated planets orbiting the MUSCLES stars share more

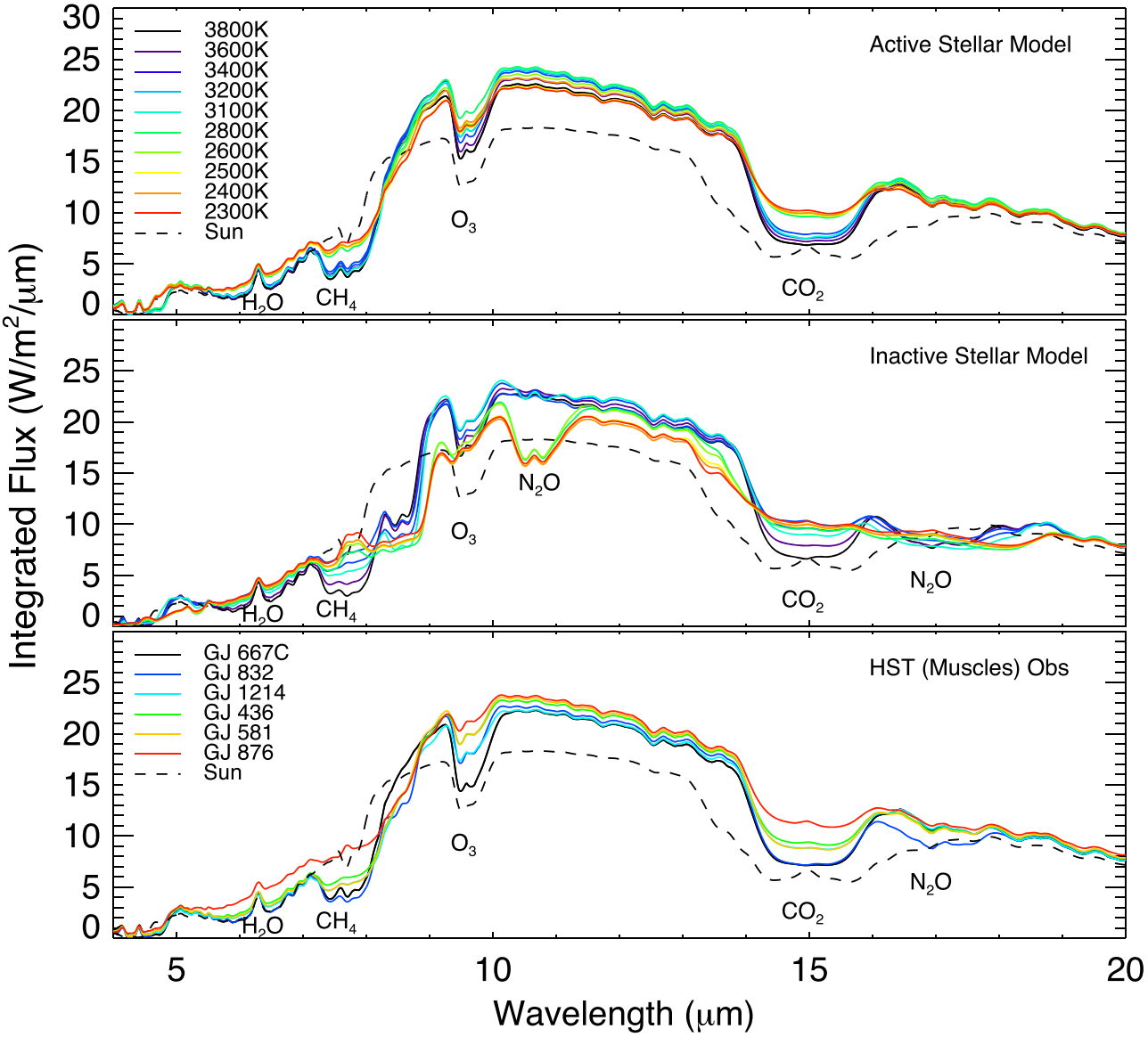


Figure 10. Smoothed, disk-integrated IR spectra at the TOA emitted by an Earth-like planet orbiting the grid of active stellar models (top), inactive stellar models (middle), and MUSCLES stars (bottom) assuming 60% Earth-analog cloud coverage model. The Earth–Sun spectrum is shown for comparison as a dashed black line.

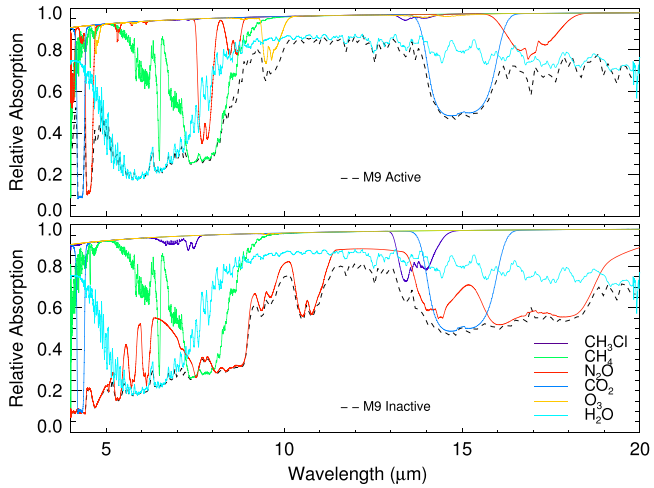


Figure 11. Individual spectral components for H_2O, CH_4, CO_2, CH_3Cl, O_3, and N_2O composing the full IR spectra (shown by a dashed black line) for an Earth-like planet orbiting an M9 active stellar model (top) and M9 inactive stellar model (bottom).

similarities with the planets orbiting the active stellar models, particularly in terms of O_3, CH_4, and N_2O concentrations, which is to be expected since they have UV fluxes detectable with *HST*.

Lyα is an important line to characterize because it is the strongest line in the FUV part of an M dwarf spectrum. We note that in addition to properly reconstructing the Lyα line, determining the base level of flux and other emission lines in the FUV and NUV is also important. This is because Lyα by itself does not significantly impact the photochemistry of an Earth-like planet atmosphere below about 60 km unless the Lyα flux exceeds the highest observed levels observed for the MUSCLES stars (see Section 3 and Figure 6).

Our present models assume a steady state. Young M dwarfs exhibit strong flares that may impact the atmosphere on timescales relevant to the photochemistry. Future work will consider activity-induced variability in an exoplanet's atmosphere. See Segura et al. (2010) for models on time-dependent behavior of biosignatures for flaring M dwarfs.

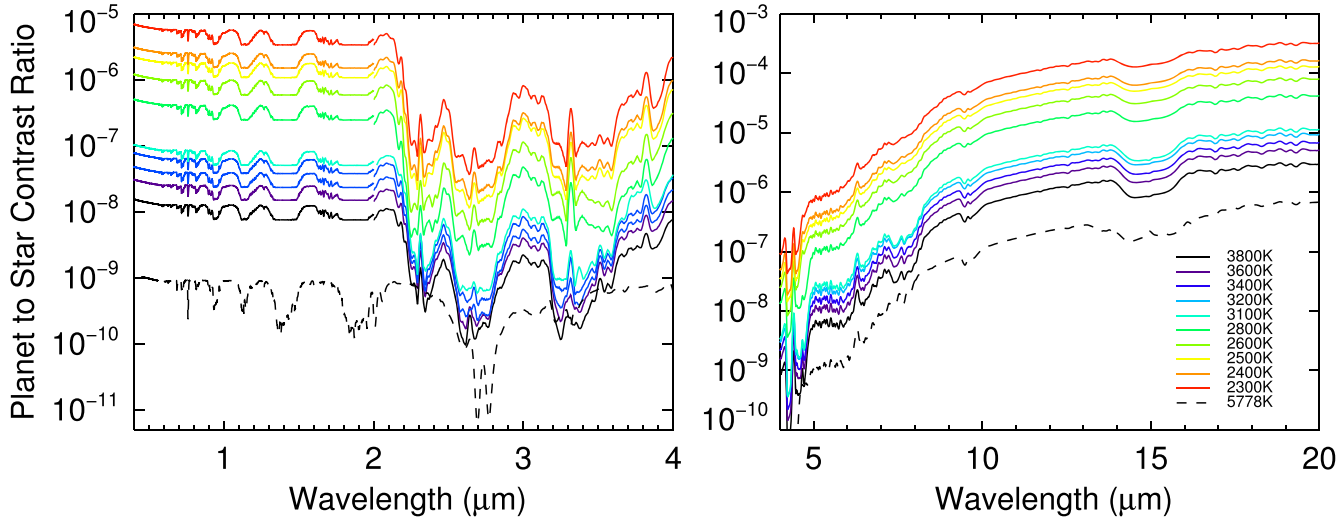


Figure 12. Contrast ratios for Earth-like planets orbiting M0–M9 stars in full illumination. Active model contrast ratios are shown here. The contrast ratios of spectral features of planets orbiting inactive M dwarfs have similar levels as active M dwarfs in our models. The black dotted lines show contrast ratios for the Earth orbiting the Sun.

6. CONCLUSIONS

We show spectral features for terrestrial atmosphere models of Earth-like planets from the visible to the IR for planets orbiting a grid of M0–M9 host stars ($T_{\rm eff}$ = 2300–3800 K) using active stellar models, inactive stellar models, and the sample of M dwarfs with observed UV fluxes. Our grid comprehensively covers the full M stellar range and activity from a proxy of an active flare star, AD Leo, to the lower limit of activity with no chromospheric contribution to the UV.

We discuss the atmospheric model results in Section 3 and the detectable spectral features with a focus on how the UV flux environment affects the emergent spectra in Section 4. Increased UV flux environments in M dwarfs are primarily a property of younger and earlier-type stars. Higher UV environments produce increased concentration of O_3 from photolysis of O_2, increased $O(^1D)$ from photolysis of O_3, increased OH from reaction of $O(^1D)$ and H_2O, decreased stratospheric H_2O, and decreased CH_4, CH_3Cl, and N_2O from photolysis and reactions with OH (see Figure 4). Very inactive M dwarfs may have extremely low UV flux levels as suggested by *GALEX* observations in the NUV. More observations are needed to determine the lower limit of fluxes in the FUV, in particular the Lyα emission. Such low levels of UV flux could lead to a buildup of molecules such as CH_4 and N_2O in the atmosphere of an Earth-like planet, with N_2O being a strong biosignature owing to a lack of photochemical sources.

Terrestrial planets orbiting early M spectral type stars are the best targets for observing biosignatures, such as O_2 or O_3 in combination with a reducing species like CH_4. Note that the O_2 line becomes increasingly difficult to detect for late M dwarfs (see Figure 8). While not observable for an exoplanet around an FGK star, N_2O may be observable at 10.7 μm or at 17 μm at Earth-level emissions for planets orbiting M dwarfs (see inactive models and model for GJ 832).

Our results provide a grid of atmospheric compositions and model spectra from the visible to the IR for *JWST* and other future space- and ground-based direct imaging and secondary eclipse missions in terms of instrument design and will help to optimize their observation strategy. The model spectra in this paper are available at www.cfa.harvard.edu/~srugheimer/Mspectra/.

We especially thank Andrew West and Evgenya L. Shkolnik for useful conversations about M dwarfs. We also would like to thank Kevin France for discussions concerning the MUSCLES database. This work has made use of the MUSCLES M dwarf UV radiation field database. We would also like to acknowledge support from DFG funding ENP KA 3142/1-1 and the Simons Foundation (290357, Kaltenegger).

The UV radiation field for AD Leo was obtained from the Multimission Archive at the Space Telescope Science Institute (MAST). STScI is operated by the Association of Universities for Research in Astronomy, Inc., under NASA contract NAS5-26555. Support for MAST for non-*HST* data is provided by the NASA Office of Space Science via grant NAG5-7584 and by other grants and contracts.

APPENDIX

GJ 667C: GJ 667C is an M3-4 dwarf at 6.8 pc (van Leeuwen 2007) with an age estimate greater than 2 Gyr (Anglada-Escudé et al. 2013b). GJ 667C has $T_{\rm eff}$ = 3350 K, [Fe/H] = −0.55, and $M = 0.330 M_{\odot} \pm 0.019$ (Anglada-Escudé et al. 2013b). Previous estimates had the effective temperature 350 K higher and the spectral designation to be M1.5 owing to assuming a higher metallicity (see Geballe et al. 2002; Anglada-Escudé et al. 2013b). We use a radius of $R = 0.35 R_{\odot}$, consistent with the luminosity $L = 0.01370\ L_{\odot}$ (Anglada-Escudé & Tuomi 2012). We merged a PHOENIX BT-Settl spectrum for $T_{\rm eff}$ = 3350 K, [Fe/H] = −0.55, $\log(g) = 5$, and $v \sin i = 3\ {\rm km\ s^{-1}}$ with the MUSCLES UV spectrum at 2800 Å. GJ 667C has less wavelength coverage than the other MUSCLES stars. We approximated the rest of the UV radiation field from the FUV and NUV SED of GJ 832, which has a similar spectral type (France et al. 2013), scaled to the distance and Lyα and Mg II emission line strength of GJ 667C.

GJ 832: GJ 832 is an M dwarf at 4.95 pc (van Leeuwen 2007) with no age estimate and is the least well characterized star in the MUSCLES program sample. It

has $T_{\rm eff}$ = 3620 K (NStED value interpolated as described in Bessell 1995), $R = 0.48 R_{\odot}$ (Johnson & Wright 1983), [Fe/H] = –0.12 (Johnson & Apps 2009), and log g = 4.7 (Bailey et al. 2008). We merged a PHOENIX BT-Settl spectrum with $T_{\rm eff}$ = 3620 K, [Fe/H] = –0.12, log g = 4.7, and $v \sin i = 3\,{\rm km\,s^{-1}}$ with the *HST* UV spectra from the MUSLES program at 2800 Å.

GJ 1214: GJ 1214 is an M6 dwarf at 14.55 ± 0.13pc (Anglada-Escudé et al. 2013a) with an age estimate of 6 ± 3 Gyr (Charbonneau et al. 2009). A more accurate parallax measurement increased the previous distance estimate by 10%, and thus the luminosity and mass have been shifted from previous values as well (Anglada-Escudé et al. 2013a). With the new parallax and luminosity, GJ 1214 has a radius of 0.211 $R_{\odot}$, $T_{\rm eff}$ = 3250 K, $M = 0.176\ M_{\odot}$ (Anglada-Escudé et al. 2013a), and [Fe/H] = +0.05 (Neves et al. 2012; Anglada-Escudé et al. 2013a). We used an upper limit of $v \sin i = 1\,{\rm km\,s^{-1}}$ (Delfosse et al. 1998; Reiners & Basri 2008; West & Basri 2009; Browning et al. 2010) and log g = 4.991 (Charbonneau et al. 2009). We merged a PHOENIX BT-Settl spectrum with $T_{\rm eff}$ = 3250 K, [Fe/H] = +0.05, log g = 4.991, and $v \sin i = 1\,{\rm km\,s^{-1}}$ with the MUSCLES UV spectrum at 2800 Å. GJ 1214 is the only MUSCLES star to have a nondetection of Lyα, and thus an upper limit is used and discussed in depth in France et al. (2013).

GJ 436: GJ 436 is an M3 dwarf at 10.1 pc (van Leeuwen 2007) with an age estimate of 6.5–9.9 Gyr (Saffe et al. 2005). GJ 436 has $T_{\rm eff}$ = 3416 K, $R = 0.455 \pm 0.018\ R_{\odot}$, and $M = 0.507$ (+0.071/–0.062) $M_{\odot}$ (von Braun et al. 2012). GJ 436 has solar metallicity, [Fe/H] = 0 (Rojas-Ayala et al. 2010), log g = 5.0 (Maness et al. 2007), and a $v \sin i < 1\,{\rm km\,s^{-1}}$ (Marcy & Chen 1992). We merged a PHOENIX BT-Settl spectrum with $T_{\rm eff}$ = 3416 K, [Fe/H] = 0, log g = 5, and $v \sin i = 1\,{\rm km\,s^{-1}}$ with the *HST* UV spectra from the MUSCLES program at 2800 Å.

Gl 581: GJ 581 is an M3 dwarf at 6.2 ± 0.1pc (van Leeuwen 2007) with age estimate of 7–11 Gyr (Selsis et al. 2007). GJ 581 has $T_{\rm eff} = 3498.0 \pm 56.0$ K, $R = 0.299 \pm 0.010\ R_{\odot}$, and log $g = 4.96 \pm 0.08$ (von Braun et al. 2011). GJ 581 has a metallicity slightly subsolar, [Fe/H] = –0.02 (Rojas-Ayala et al. 2010), and an upper limit on $v \sin i \leqslant 2.1\,{\rm km\,s^{-1}}$ (Delfosse et al. 1998). We merged a PHOENIX BT-Settl spectrum with $T_{\rm eff}$ = 3498 K, [Fe/H] = –0.02, log g = 4.96, and $v \sin i = 2.1\,{\rm km\,s^{-1}}$ (Correia et al. 2010) with the MUSCLES UV spectrum at 2800 Å.

GJ 876: GJ 876 is an M dwarf at 4.69 pc (van Leeuwen 2007) with an age 0.1–5 Gyr (Correia et al. 2010). GJ 876 has $T_{\rm eff} = 3129 \pm 19$ K and $R = 0.3761 \pm 0.0059\ R_{\odot}$ (von Braun et al. 2014). We merged a PHOENIX BT-Settl spectrum with $T_{\rm eff}$ = 3129 K, [Fe/H] = +0.19 (Rojas-Ayala et al. 2012), log g = 4.89 (Bean et al. 2006), and $v \sin i = 1.38\,{\rm km\,s^{-1}}$ (Correia et al. 2010) with the MUSCLES UV spectrum at 2800 Å.

REFERENCES

Allard, F. 2014, Proc. IAU Symp. 299, Exploring the Formation and Evolution of Planetary Systems, ed. M. Booth, B. C. Matthews & J. R. Graham (Cambridge: Cambridge Univ. Press), 271
Anglada-Escudé, G., Rojas-Ayala, B., Boss, A. P., Weinberger, A. J., & Lloyd, J. P. 2013a, A&A, 551, A48
Anglada-Escudé, G., & Tuomi, M. 2012, A&A, 548, A58
Anglada-Escudé, G., Tuomi, M., Gerlach, E., et al. 2013b, A&A, 556, A126
Bailey, J., Butler, R. P., Tinney, C. G., et al. 2008, ApJ, 690, 743
Batalha, N. M., Rowe, J. F., Bryson, S. T., et al. 2013, ApJS, 204, 24
Bean, J. L., Benedict, G. F., & Endl, M. 2006, ApJL, 653, L65
Beichman, C., Lawson, P., Lay, O., et al. 2006, Proc. SPIE, 6268, 626805
Beichman, C. A., Woolf, N. J., & Lindensmith, C. A. 1999, The Terrestrial Planet Finder (TPF): A NASA Origins Program to Search for Habitable Planets (Pasadena, CA: JPL Publications)
Bessell, M. S. 1995, in Proc. ESO Workshop, The Bottom of the Main Sequence—and Beyond, ed. C. G. Tinney (Berlin: Springer-Verlag), 123
Borucki, W. J., Agol, E., Fressin, F., et al. 2013, Sci, 340, 587
Borucki, W. J., Koch, D. G., Basri, G., et al. 2011, ApJ, 736, 19
Broecker, W. S. 1982, GeCoA, 46, 1689
Browning, M. K., Basri, G., Marcy, G. W., West, A. A., & Zhang, J. 2010, AJ, 139, 504
Cash, W. 2006, Natur, 442, 51
Charbonneau, D., Berta, Z. K., Irwin, J., et al. 2009, Natur, 462, 891
Correia, A. C. M., Couetdic, J., Laskar, J., et al. 2010, A&A, 511, A21
Delfosse, X., Forveille, T., Perrier, C., & Mayor, M. 1998, A&A, 331, 581
Deming, D., Seager, S., Winn, J., et al. 2009, PASP, 121, 952
Des Marais, D. J., Harwit, M. O., Jucks, K. W., et al. 2002, AsBio, 2, 153
Domagal-Goldman, S. D., Segura, A., Claire, M. W., Robinson, T. D., & Meadows, V. S. 2014, ApJ, 792, 90
Dressing, C. D., & Charbonneau, D. 2013, ApJ, 767, 95
Forster, P., Ramaswamy, V., Artaxo, P., et al. 2007, in Climate Change 2007: The Physical Science Basis. Contribution of Working Group I to the Fourth Assessment Report of the Intergovernmental Panel on Climate Change, ed. S. Solomon et al. (Cambridge: Cambridge Univ. Press), ch. 2
France, K., Froning, C. S., Linsky, J. L., et al. 2013, ApJ, 763, 149
Gardner, J. P., Mather, J. C., Clampin, M., et al. 2006, SSRv, 123, 485
Geballe, T. R., Knapp, G. R., Leggett, S. K., et al. 2002, ApJ, 564, 466
Grenfell, J. L., Gebauer, S. V., Paris, P., Godolt, M., & Rauer, H. 2014, Planet. Space Sci., 98, 66
Guzmán-Marmolejo, A., Segura, A., & Escobar-Briones, E. 2014, AsBio, 13, 550
Haqq-Misra, J. D., Domagal-Goldman, S. D., Kasting, P. J., & Kasting, J. F. 2008, AsBio, 8, 1127
Hawley, S. L., Gizis, J. E., & Reid, I. N. 1996, AJ, 112, 2799
Hu, R., Seager, S., & Bains, W. 2012, ApJ, 761, 166
Jenkins, J. S., Ramsey, L. W., Jones, H. R. A., et al. 2009, ApJ, 704, 975
Johnson, H. M., & Wright, C. D. 1983, ApJS, 53, 643
Johnson, J. A., & Apps, K. 2009, ApJ, 699, 933
Jones, D., & West, A. A. 2015, ApJ, submitted
Kaltenegger, L. 2010, ApJL, 712, L125
Kaltenegger, L., Fridlund, M., & Karlsson, A. 2006, Ap&SS, 306, 147
Kaltenegger, L., & Sasselov, D. 2010, ApJ, 708, 1162
Kaltenegger, L., & Sasselov, D. 2011, ApJL, 736, L25
Kaltenegger, L., Sasselov, D., & Rugheimer, S. 2013, ApJL, 775, L47
Kaltenegger, L., & Traub, W. A. 2009, ApJ, 698, 519
Kaltenegger, L., Traub, W. A., & Jucks, K. W. 2007, ApJ, 658, 598
Kasting, J. F., & Ackerman, T. P. 1986, Sci, 234, 1383
Kasting, J. F., Holland, H. D., & Pinto, J. P. 1985, JGR, 90, 10497
Kasting, J. F., Pollack, J. B., & Crisp, D. 1984, JAtC, 1, 403
Kharecha, P., Kasting, J. F., & Siefert, J. 2005, Geobiology, 3, 53
Kiang, N. Y., Segura, A., Tinetti, G., et al. 2007, AsBio, 7, 252
Kitzmann, D., Patzer, A. B. C., von Paris, P., Godolt, M., & Rauer, H. 2011a, A&A, 531, A62
Kitzmann, D., Patzer, A. B. C., von Paris, P., Godolt, M., & Rauer, H. 2011b, A&A, 534, A63
Linsky, J. L., France, K., & Ayres, T. 2013, ApJ, 766, 69
Lovelock, J. E. 1975, RSPSB, 189, 167
Maness, H. L., Marcy, G. W., Ford, E. B., et al. 2007, PASP, 119, 90
Marcy, G. W., & Chen, G. H. 1992, ApJ, 390, 550
Miguel, Y., Kaltenegger, L., Linsky, J. L., & Rugheimer, S. 2015, MNRAS, 446, 345
Neves, V., Bonfils, X., Santos, N. C., et al. 2012, A&A, 538, A25
Pavlov, A. A., & Kasting, J. F. 2002, AsBio, 2, 27
Pavlov, A. A., Kasting, J. F., Brown, L. L., Rages, K. A., & Freedman, R. 2000, JGR, 105, 11981
Quintana, E. V., Barclay, T., Raymond, S. N., et al. 2014, Sci, 344, 277
Rauer, H., Gebauer, S. v., Paris, P., et al. 2011, A&A, 529
Reiners, A., & Basri, G. 2008, ApJ, 684, 1390
Ricker, G. R., Winn, J. N., Vanderspek, R., et al. 2014, Proc. SPIE, 9143, 914320
Rodler, F., & López-Morales, M. 2014, ApJ, 781, 54
Rojas-Ayala, B., Covey, K. R., Muirhead, P. S., & Lloyd, J. P. 2010, ApJL, 720, L113

Rojas-Ayala, B., Covey, K. R., Muirhead, P. S., & Lloyd, J. P. 2012, ApJ, 748, 93
Rugheimer, S., Kaltenegger, L., Zsom, A., Segura, A., & Sasselov, D. 2013, AsBio, 13, 251
Saffe, C., Gómez, M., & Chavero, C. 2005, A&A, 443, 609
Sagan, C., Thompson, W. R., Carlson, R., Gurnett, D., & Hord, C. 1993, Natur, 365, 715
Schindler, T. L., & Kasting, J. F. 2000, Icar, 145, 262
Seager, S., Schrenk, M., & Bains, W. 2012, AsBio, 12, 61
Segura, A., Kasting, J. F., Meadows, V., et al. 2005, AsBio, 5, 706
Segura, A., Krelove, K., Kasting, J. F., et al. 2003, AsBio, 3, 689
Segura, A., Meadows, V. S., Kasting, J. F., Crisp, D., & Cohen, M. 2007, A&A, 472, 665
Segura, A., Walkowicz, L. M., Meadows, V., Kasting, J., & Hawley, S. 2010, AsBio, 10, 751
Selsis, F. 2000, in ESA Special Publication 451, Darwin and Astronomy: The Infrared Space Interferometer, ed. B. Schürmann (Noordwijk: ESA), 133
Selsis, F., Kasting, J. F., Levrard, B., et al. 2007, A&A, 476, 1373
Shkolnik, E. L., & Barman, T. S. 2014, ApJ, in press (arXiv:1407.1344)
Snellen, I. A. G., de Kok, R. J., le Poole, R., Brogi, M., & Birkby, J. 2013, ApJ, 764, 182
Tian, F., France, K., Linsky, J. L., Mauas, P. J. D., & Vieytes, M. C. 2014, E&PSL, 385, 22
Toon, O. B., McKay, C. P., Ackerman, T. P., & Santhanam, K. 1989, JGR, 94, 16287
Traub, W. A., Levine, M., Shaklan, S., et al. 2006, Proc. SPIE, 6268, 62680T
Traub, W. A., & Stier, M. T. 1976, ApOpt, 15, 364
Udry, S., Bonfils, X., Delfosse, X., et al. 2007, A&A, 469, L43
van Leeuwen, F. 2007, A&A, 474, 653
von Braun, K., Boyajian, T. S., Kane, S. R., et al. 2011, ApJL, 729, L26
von Braun, K., Boyajian, T. S., Kane, S. R., et al. 2012, ApJ, 753, 171
von Braun, K., Boyajian, T. S., van Belle, G. T., et al. 2014, MNRAS, 438, 2413
Walkowicz, L. M., & Hawley, S. L. 2009, AJ, 137, 3297
West, A. A., & Basri, G. 2009, ApJ, 693, 1283
West, A. A., Hawley, S. L., Walkowicz, L. M., et al. 2004, AJ, 128, 426
West, A. A., Morgan, D. P., Bochanski, J. J., et al. 2011, AJ, 141, 97
Wood, B. E., Redfield, S., Linsky, J. L., Müller, H.-R., & Zank, G. P. 2005, ApJS, 159, 118
Wordsworth, R., & Pierrehumbert, R. 2014, ApJL, 785, L20
Wordsworth, R. D., Forget, F., Selsis, F., et al. 2011, ApJL, 733, L48